Thesis for the Degree of
Doctor of Philosophy in Engineering

Efficient Electromagnetic Imaging of the Vadose Zone Using Cross-Borehole Radar

by
Hannuree Jang

Department of Energy Resources Engineering
The Graduate School
Pukyong National University

February 2012

Efficient Electromagnetic Imaging of the Vadose Zone Using Cross-Borehole Radar

(시추공간 레이더에 의한 불포화층의 효율적인 전자기 영상화)

Advisor: Prof. Hee Joon Kim

by

Hannuree Jang

A thesis submitted in partial fulfillment of the requirements

for the degree of

Doctor of Philosophy in Engineering

in Department of Energy Resources Engineering, The Graduate School,

Pukyong National University

February 2012

Efficient Electromagnetic Imaging of the Vadose Zone Using Cross-Borehole Radar
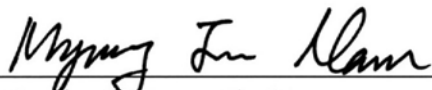
A dissertation
by
Hannuree Jang

Approved by:

_____
(Chairman) Jeong-Gi Um

_____
(Member) Yosoon Choi

_____
(Member) Seong-Jun Cho

_____
(Member) Myung Jin Nam

_____
(Member) Hee Joon Kim

February 2012

Contents

List of figures

iv

v

Efficient Electromagnetic Imaging of the Vadose Zone Using Cross-Borehole Radar

Hannuree Jang

Department of Energy Resources Engineering, The Graduate School,

Pukyong National University

Abstract

Ground-penetrating radar (GPR) is an effective tool for imaging the spatial distribution of water content. Cross-borehole GPR has been widely used to characterize the shallow subsurface and to monitor hydrogeologic processes. To investigate an infiltration process in the vadose zone, an artificial groundwater infiltration test was conducted in Nagaoka, Japan. Time-lapse cross-borehole GPR data were collected using zero-offset profiling (ZOP) mode. The infiltration process was observed as a variation of GPR traveltimes, which can be transformed into a dielectric constant, and further converted to volumetric water content. Since electromagnetic (EM) wave velocities in the vadose zone are largely controlled by variations in water content, an increase in traveltime is interpreted as an increase in saturation.

High-frequency EM wave propagation associated with borehole GPR is a complicated phenomenon. To improve the understanding of the governing physical processes, we employ a finite-difference time-domain (FDTD) solution of Maxwell's equations in cylindrical coordinates. This approach allows us to model the full EM wavefield associated with crosshole GPR surveys. Furthermore, the use of cylindrical coordinates is computationally efficient, correctly emulates the three-dimensional (3D) geometrical spreading characteristics of the wavefield, and is an effective way to discretise explicitly small-diameter boreholes. Numerical experiments show that the existence of a water-filled borehole can give rise to a strong waveguide effect which affects the transmitted waveform, and that excitation of this waveguide effect depends

on the diameter of the borehole and the length of the antenna.

In the test zone, the infiltrated water penetrated downward with an average velocity of about 2.7 m/h. The FDTD method using 2D cylindrical coordinates is applied to simulate radargrams associated with the advancing wetting front and to quantify the effects of critical refraction. A standard ZOP mode for which all first-arrivals are assumed to be direct waves results in an underestimation of water content in the transition zone above the wetting front. As a result, correct velocity analysis requires identification of first-arriving critically refracted waves from the traveltime profile to accurately determine a water content profile.

The standard ZOP analysis results in an underestimation of the dielectric constant because of the existence of critically refracted waves. We present an efficient algorithm using the maximum first-cycle amplitude to approximately determine the traveltime of direct arrival, deriving a dielectric constant model more accurately than the standard ZOP analysis from ZOP data. Tests on synthetic and real field data show that the proposed approach is effective in building accurate water content profile without iterative calculations as in the standard ZOP analysis.

We further present an approach to extract accurate information about the hydrogeologic process in the vadose zone from ZOP data. This approach is based on a least-squares inversion method using singular-value decomposition, in which the FDTD forward modeling is used for computing EM wave fields on 2D cylindrical coordinates. The inversion approach is validated using a synthetic example and applied to the field data. We can successfully estimate the variation of soil water content during infiltration in the Nagaoka site from the reconstructed dielectric constant models. The inversion results show that the saturation information is useful to assess hydrogeologic properties of the test soil zone.

Keywords: ground-penetrating radar (GPR), cross-borehole, time-lapse, zero-offset profiling (ZOP), cylindrical coordinates, finite difference time domain (FDTD), vadose zone, dielectric constant, water content

Chapter 1. Introduction

1.1. Background and motivation

Preservation of environment and water resources has become a primary concern for sustainable development of our society. This can be achieved through a precise understanding of hydrological processes, for which observation and monitoring play a prominent role. In this regard, the characterization of the spatiotemporal distribution of soil water content is required in various areas, such as environmental and agricultural engineering, because this parameter controls major processes of the hydrological cycle including the partition of precipitation into infiltration and runoff, evaporation, or energy exchanges between the earth and atmosphere.

Direct measurement of soil water content is invasive and generally inadequate to yield sufficient spatial coverage for basin-scale investigations, based on drilling. In addition, direct sampling disturbs the soil, restricting the ability to monitor transient processes. It is difficult to use small-scale samples to describe representative field-scale properties, particularly in loose sediments (Cassiani et al., 2006). The development of geophysical techniques for characterization of the subsurface has been very rapid over the past couple of decades. Cross-borehole ground-penetrating radar (GPR) has been increasingly used in hydrogeologic studies on the shallow subsurface. GPR traveltimes are sensitive to changes in dielectric constant and can thus be used to measure soil water content (Huisman et al., 2003), provided that an accurate petrophysical model is given that relates the composite dielectric constant to the volumetric water content (Davis and Annan, 1989; Topp et el., 1980). This approach allows for state estimation, and if time-lapse cross- borehole traveltime tomography is employed, the changes in the inferred water content distribution can be used as the basis for hydrological interpretation (Binley et al., 2002).

Near-surface, environmental investigations often require monitoring of the spatial distribution of water content. Water content estimates are needed to model and

predict pollutant transport through the vadose zone, and to subsequently design an efficient and reliable remediation plan. Time-lapse GPR has been used successfully to image mass transport such as vegetable oil emulsion (Lane et al., 2006) and saline water (Chang et al., 2006). The time-lapse imaging at field sites can be divided into three main modes of operation: surface-based or single-borehole reflection surveying (Truss et al. 2007), surface-to-borehole surveying (Cassiani et al., 2004), and cross-borehole surveying (Binley et al., 2001; 2002; Kowalsky et al., 2005). Among these modes, time-lapse cross-borehole GPR has gained popularity for monitoring water content changes, thanks to its high resolution capabilities (Binley et al., 2001; 2002; Alumbaugh et al., 2002).

Over the past decade, borehole GPR has become an increasingly popular tool for noninvasive, high-resolution imaging of the shallow subsurface. Applications of this technique include delineation of ore bodies (Fullagar et al., 2000), location of underground tunnels and voids (Olhoeft, 1988; Moran and Greenfield, 1993), mapping fractures in bedrock (Olsson et al., 1992; Day-Lewis et al., 2003), and estimation of subsurface lithology and hydrogeological properties (Alumbaugh et al., 2002; Moysey and Knight, 2004; Tronicke et al., 2004). Due to the strong correlation of electromagnetic (EM) wave velocity with water content in the subsurface, the technique is commonly used to detect differences in porosity in the saturated zone, as well as difference in soil water retention and thus grain size in the vadose zone (Truss et al., 2007; Irving et al., 2007).

Crosshole GPR tomography is identical in principle to seismic tomography. A transmitter antenna, moved to numerous locations in one borehole, radiates high-frequency EM pulses that are recorded by a receiver antenna, which is moved down a second borehole. In crosshole GPR, two acquisition geometries are usually employed: multi-offset gathering (MOG, tomography geometry) and zero-offset profiling (ZOP, level-run geometry) (Binley et al., 2001; Lane et al., 2006). MOG offers multi-dimensional imaging through high-resolution tomography, but is relatively slow due to the large number of measurements (Alumbaugh et al., 2002). Tomographic schemes typically rely on some kind of ray approximation of the EM waves. Straight-ray

algorithms give reliable results if the velocity variations in the medium are moderate. If strong velocity variations are expected, algorithms that take bending of the rays into account will produce more reliable results. In contrast to tomography data, ZOP data do not require tomographic inversion, and the EM wave velocity is calculated for a known antenna separation, assuming that the first-arriving energy travels along a direct path from the transmitter to the receiver. This assumption, however, can give rise to erroneous velocity estimates if refracted waves are first to arrive (Hammon et al., 2002; Huisman et al., 2003; Rucker and Ferré, 2003; 2004).

Most commonly, inversion of the resulting data is accomplished by assuming that the propagating radar energy can be modeled by infinite-frequency rays that join the centers of the antennas. Under this assumption, first-break traveltimes and amplitudes of the data can be used to determine the distribution of subsurface EM-wave velocity and attenuation. The resulting ray-based tomographic images of the subsurface, however, are limited in resolution to approximately the width of the first Fresnel zone associated with the propagating pulse bandwidth (Williamson and Worthington, 1993). In order to improve resolution, we require modeling algorithms that account for more detailed physical aspects of the crosshole GPR experiment, such as wave propagation and antenna behavior. These algorithms can be employed in waveform-based inversion strategies that use all of the recorded data to determine subsurface properties (e.g., Pratt and Worthington, 1988; Zhou et al., 1995).

There are a number of approaches to crosshole GPR modeling. None of these, however, allow for the simulation of both antenna transmission and reception in heterogeneous media. Sato and Thierbach (1991), for example, analytically modeled a crosshole GPR experiment using an expression for the current on an insulated dipole antenna derived by King and Smith (1981). Although their approach gives much insight into the effects of antenna and system parameters on recorded GPR wavelets, it requires a homogeneous medium between the boreholes and that the antennas are each in the far field of the other. In addition, the expression used for the antenna current is invalid for the case of water-filled boreholes and is thus only suitable for modeling in the vadose zone. Holliger and Bergmann (2002), on the other hand, numerically

modeled crosshole GPR using a finite-difference time-domain (FDTD) approach in two-dimensional (2D) cylindrical coordinates. In their formulation, only the transmitter borehole was included in the model, and the antennas were simulated as point vertical electric dipoles. Ernst et al. (2006) further developed this algorithm to allow for detailed modeling of a realistic, finite-length transmitter antenna. Ellefsen and Wright (2005) employed a similar approach to examine the radiation patterns of realistic borehole GPR antennas. With these methods, much can be learned about the effects of the borehole, subsurface heterogeneity, and antenna characteristics on crosshole GPR radiation.

This dissertation focuses on extracting of accurate information about the hydrogeologic process in the vadose zone from ZOP data. More specifically, an artificial groundwater infiltration test was carried out in Nagaoka City, Japan (Kuroda et al., 2007; 2008), and time-lapse cross-borehole measurements were acquired to monitor the infiltration process in the vadose zone. In the experiment, time-efficient ZOPs were utilized because a large amount of water was released in a short period of time and rapid water migration into the vadose zone was expected. In ZOP mode, an EM wave velocity is usually calculated for a known antenna separation, assuming that the first-arriving EM energy travels along a straight path from the transmitter to the receiver. This standard ZOP analysis, however, can give rise to erroneous velocity estimates if refracted waves are first to arrive (Huisman et al, 2003; Rucker and Ferre, 2004), and results in an underestimation of water content estimates in the transition zone above a wetting front (Kuroda et al., 2009; Jang et al., 2011a; 2011b). In this thesis, we introduce three efficient methods to solve the problem of underestimation. A significant part of this thesis is devoted to the numerical modeling algorithm, which is accomplished using the FDTD method in 2D cylindrical coordinates, to simulate cross-borehole GPR wavefields in the vadose zone during the infiltration process.

1.2. Thesis overview

This dissertation consists of seven chapters. Each chapter has been prepared as a stand-alone paper for submission to a peer-reviewed scientific journal.

Chapter 1 presents background, motivation and overview of this thesis.

In Chapter 2, we summarize an artificial groundwater infiltration test was carried out in Nagaoka, Japan (Kuroda et al., 2007; 2009). Time-lapse cross-borehole measurements were made to monitor the infiltration process in the vadose zone. In the experiment, time-efficient ZOPs were utilized because a large amount of water was released in a short period of time and rapid water migration into the vadose zone was expected. In a transition zone such that soil water content varies significantly with depth, critically refracted waves may arrive before direct waves. The standard ZOP analysis for which all first arrivals are assumed to be direct waves results in an underestimation of water content in the transition zone above a wetting front (Kuroda et al., 2009).

In Chapter 3, we present an algorithm to efficiently simulate cross-borehole GPR transmission in heterogeneous media. This is accomplished using FDTD modeling in 2D cylindrical coordinates. The algorithm can be easily implemented using a perfectly matched layer (PML) for absorbing boundaries, frequency-dependent media, and a finite-length transmitter antenna. The approach allows us to systematically explore the effects of various complicating factors on the radiated GPR signals. In this dissertation, we examine waveguide effects due to the existence of a water-filled borehole, and show that guided waves are affected by the diameter of the borehole, the length of the antenna and the shape of transmitting signal. This chapter was published in the journal *Exploration Geophysics* (Jang et al., 2007).

In Chapter 4, we apply a method to determine the water content above the wetting front using the slope analysis of the traveltime versus depth profile to overcome the problem of underestimation of water content as mentioned above. To simulate GPR wavefields and evaluate the dielectric permittivity accurately in the vadose zone, the FDTD solution of Maxwell's equations 2D cylindrical coordinates

(Jang et al., 2007) is applied. This chapter was published in the journal *Applied Geophysics* (Kuroda et al., 2009).

Chapter 5 again focuses on interpreting cross-borehole GPR data obtained in the vadose zone. The approach using the slope analysis of the traveltime versus depth profile to solve the problem of underestimation in dielectric constant estimates. The slope analysis, however, is applicable only in presence of layers having a uniform water content. We present an efficient algorithm to obtain an accurate dielectric constant model from ZOP data. The algorithm uses the maximum first-cycle amplitude to approximately determine the arrival time of direct waves. This chapter was published in the journal *IEEE Geoscience and Remote Sensing letters* (Jang et al., 2011a).

In Chapter 6, we present an inversion approach to derive an accurate dielectric constant model from ZOP data. The method using the maximum first-cycle amplitude to approximately derive the direct-wave arrival time is marginally reduced the underestimation in water content estimates. The final method is supposed to be most accurate in building a dielectric constant model from first-arrival traveltimes if a forward model can express critically refracted waves accurately. This approach is based on a least-squares inversion method using singular value decomposition. This chapter was published in the journal *IEEE Transactions on Geoscience and Remote Sensing* (Jang et al., 2011b).

In the concluding chapter (Chapter 7), we briefly discuss and summarize for the previous five chapters. Then some possible ways for future research are proposed based on the work presented in this thesis.

Chapter 2. Time-lapse borehole radar monitoring of an infiltration experiment in the vadose zone

2.1. Time-lapse Cross-borehole Experiment

An artificial groundwater recharge test was conducted in Nagaoka City in Niigata Prefecture, Japan (Kuroda et al., 2006). In this experiment, borehole GPR measurements were collected to monitor the infiltration process in the vadose zone. A schematic diagram is shown in Fig. 2.1 to illustrate the spatial arrangement of the infiltration pit and the boreholes. The top 2 m of soil consisted of loam, and the subsoil was sand and gravel. The groundwater table was located at approximately 10 m below the ground surface.
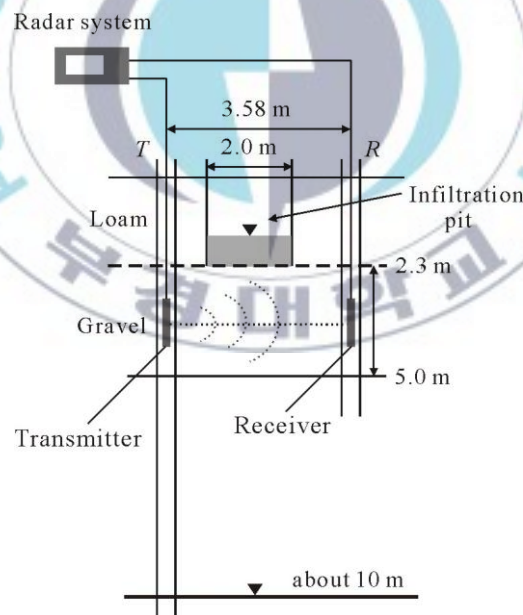
Fig. 2.1. Schematic of an artificial groundwater recharge test in a vadose zone.

During the infiltration experiment, water was applied from a 2 m by 2 m wooden tank whose base was set at a depth of 2.3 m. The total volume of water injected into the soil was 2 m³ (2 m × 2 m × 0.5 m), requiring approximately 40 min for all water to flow out. Two boreholes were located on both sides of the tank with a separation of 3.58 m. Each borehole was PVC cased, with a diameter of 7 cm. The GPR data were acquired using a GSSI SIR10 system with 1 m long borehole antennas with a dominant frequency of 110 MHz. The transmitter and receiver antennas were placed in boreholes T (11 m depth) and R (5.7 m depth), respectively.

In the experiment, time-efficient ZOPs were utilized because relatively rapid water migration into the gravel layer was expected. In ZOP mode, both transmitter and receiver antennas are lowered to a common depth. ZOP measurements represent horizontal averages of EM properties between boreholes at different depths. GPR data were collected every 0.1 m at depths of 2.3 – 5.0 m. It required approximately two minutes covering the whole depth range. A total of 25 profiles were obtained during the experiment that lasted for 322 min.

Three radargram profiles acquired from this experiment are shown in Fig. 2.2. First arrival traveltimes range from 36 – 38 ns in the initial, unsaturated state (Fig. 2.2a), and 42 – 44 ns in the final state (Fig. 2.2c), which is considered to be fully saturated. In the intermediate state of 51 – 53 min after infiltration, first arrival traveltimes are almost identical to the initial state at depths below 4 m (Fig. 2.2b). In the zone shallower than 4 m, first arrival traveltimes are delayed; the shallower the depth, the longer the traveltime. This delay is caused by increased wetting in the vadose zone (transition zone).

2.2. Standard ZOP method

The infiltration process may not be 1D because the vadose zone is heterogeneous. Since the standard ZOP method relies on determining the velocity of an EM wave that follows a straight path from the transmitter to the receiver, we approximate the

infiltration process with ZOPs as 1D (Fig 2.3). Fig. 2.4 demonstrates vertical profiles of first arrival times of radargrams shown in Fig. 2.2. In the illustration, the volumetric water content at a specific depth is estimated based on the following procedure. By assuming a straight raypath, a first arrival time is used to calculate velocity (v) as $v = d/t$, where d is the offset distance between transmitter and receiver and t is the
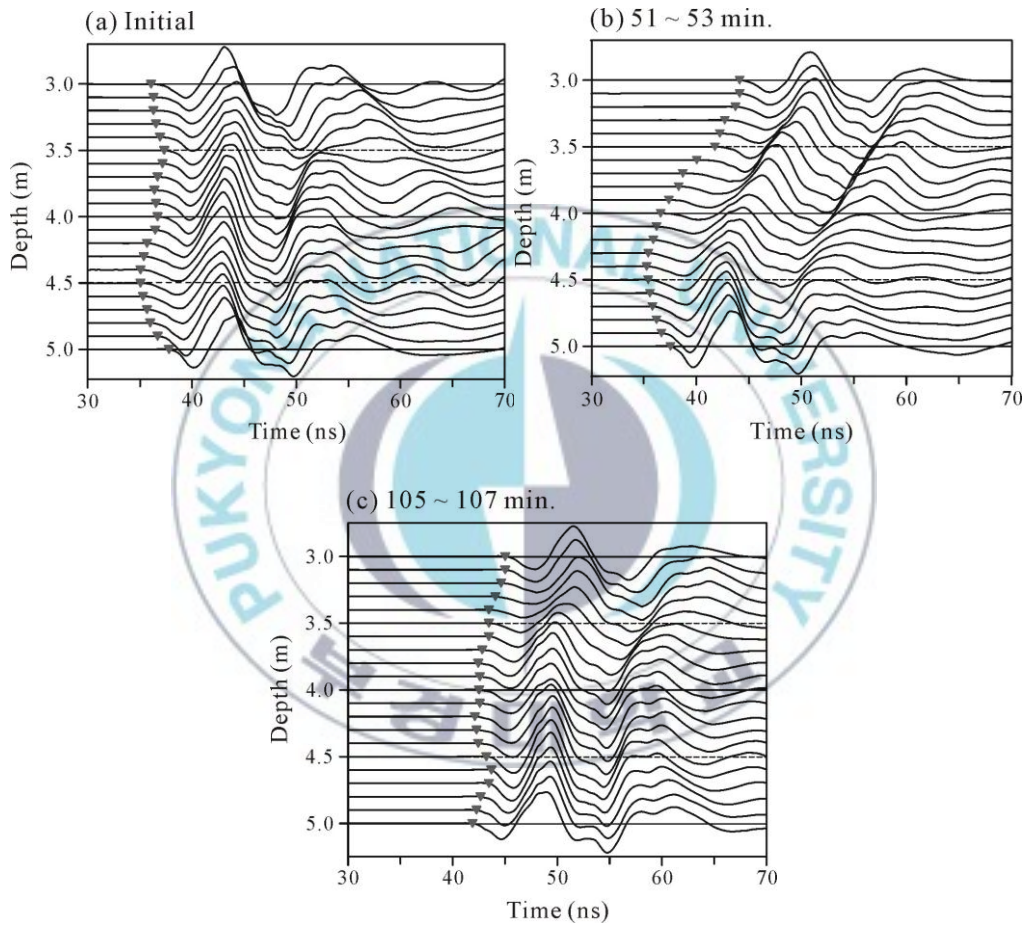
Fig. 2.2. Radargrams observed during the infiltration test: before infiltration (a), about 52 minutes after infiltration (b), and about 106 minutes after infiltration (c). Triangles show first arrival times picked.

- 9 -
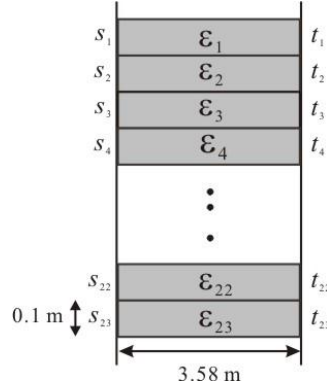
Fig. 2.3. A schematic dielectric constant model used for interpreting ZOP data.

traveltime. By further assuming that frequency-dependent dielectric loss is relatively small (Davis and Annan, 1989), the apparent dielectric constant K_a is obtained from

$$K_a = (c/v)^2,$$ (2.1)

where $c = 0.3$ m/ns is the EM wave velocity in free space. Finally, volumetric water content θ can be estimated by substituting K_a into the empirical Topp's equation (Topp et al., 1980)

$$\theta = -0.053 + 0.029K_a - 5.5 \times 10^{-4} K_a^2 + 4.3 \times 10^{-6} K_a^3.$$ (2.2)

Although this relationship does not hold well for soils with high clay content, it is in good agreement with unconsolidated materials at high water content (Robinson et al., 2003; Huisman et al., 2003; Bano, 2004). In order to verify the Topp's equation, Kuroda et al. (2007) compared volumetric water contents from core samples extracted at depths of 2.3 – 2.5 m and GPR data, and found a good agreement.

Spatial and temporal variations of volumetric water content are derived using all first arrival times collected during the infiltration experiment (Fig. 2.4). This

illustration clearly shows the movement of the wetting front in the test zone during the infiltration process. The water content varies sharply from unsaturated state (left lower side) to saturated state (right upper side). The zone exhibiting significant changes can be interpreted as a transition zone. An average downward velocity of infiltrated water in the test zone is estimated to be about 2.7 m/h as the boundary between the unsaturated and transition zones (Fig. 2.5).

Near the wetting front, critically refracted energy that travels along the boundary between the perturbed and the unperturbed zones with the velocity of an EM
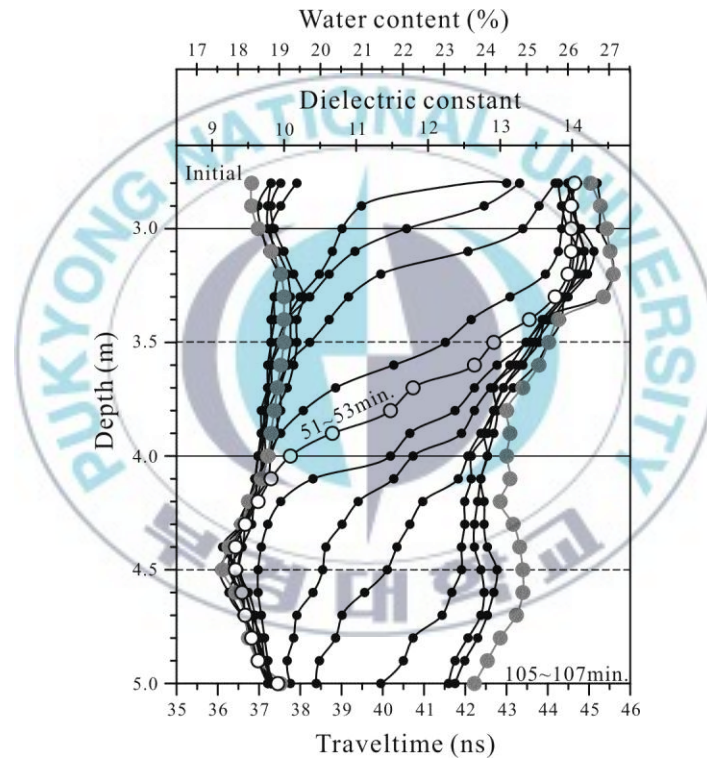
Fig. 2.4. First arrival times picked from time-lapse ZOP of radargrams obtained from the infiltration experiment. EM-wave velocities estimated by first arrival times are transformed into apparent dielectric constants and further converted to volumetric water contents.
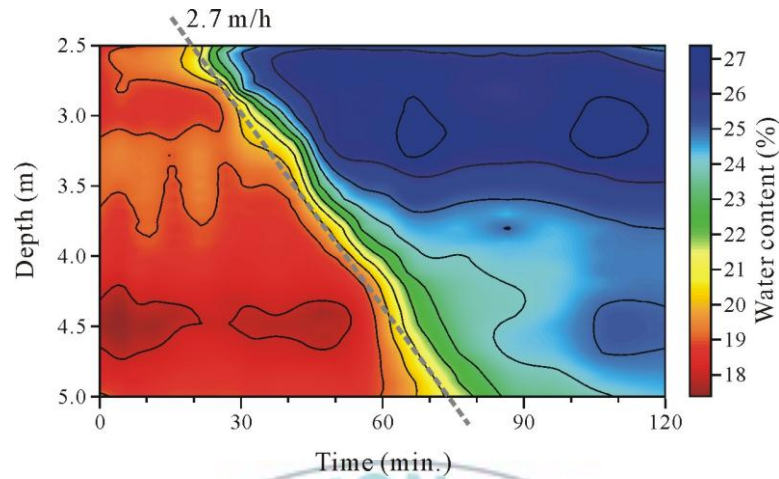
Fig. 2.5. A map showing spatiotemporal variations of volumetric water contents in the test zone during the infiltration process. The infiltrated water penetrates vertically with a velocity of about 2.7 m/h.

wave in the unperturbed zone may arrive prior to direct waves that travel through the perturbed or transition zone. If the critically refracted waves are mistakenly interpreted to be direct waves, the water content will be underestimated. As a result, the water content near the wetting front cannot be determined accurately using the standard ZOP method.

If GPR antennas are located within a high water content (slow) layer that is adjacent to a lower water content (fast) layer, critically refracted waves may arrive before direct waves. The standard ZOP analysis in which all first arrivals are assumed to be direct waves results in a significant underestimation of water content estimates in the transition zone (Binley, 2001; Deiana, 2007; 2008). To obtain a more accurate dielectric constant model, we introduce three methods: 1) identification of critically refracted waves (Chapter 4), 2) estimation of direct-wave arrival times (Chapter 5), and 3) velocity inversion of first-arrival traveltimes (Chapter 5). To simulate cross-borehole GPR wavefields and evaluate the dielectric permittivity accurately in the

vadose zone, we introduce a FDTD solution of Maxwell's equations in 2D cylindrical coordinates (Chapter 3).

2.3. Summary

An artificial groundwater recharge test was performed in Nagaoka, Japan. Time-lapse ZOP borehole GPR data were acquired to monitor the infiltration process in the vadose zone. The infiltration process is clearly observed as a variation of EM wave velocities, which can be transformed into dielectric constants and further converted to water contents using Topp's equation. GPR responses in the vadose zone are largely controlled by variations in water saturation. An increase in traveltimes can be attributed to an increase in water saturation, and the standard ZOP method allows us to estimate that the wetting front moves downward with an average velocity of about 2.7 m/h in the test zone.
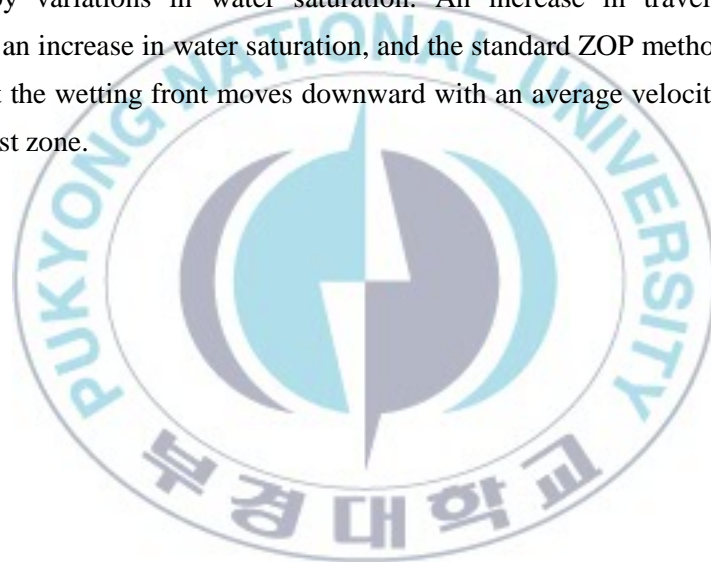
Chapter 3. Numerical modeling of cross-borehole radar measurements

3.1. Introduction

Over the past decade, borehole GPR has become increasingly popular as a tool for high-resolution imaging of the shallow subsurface. Applications of this technique include delineation of ore bodies (Fullagar et al., 2000), location of underground tunnels and voids (Olhoeft, 1988; Moran and Greenfield, 1993), mapping fractures in bedrock (Olsson et al., 1992; Day-Lewis et al., 2003), and estimation of subsurface lithology and hydrogeological properties using field- or laboratory-derived petrophysical relationships (Alumbaugh and Chang, 2002; Moysey and Knight, 2004; Tronicke et al., 2004).

Crosshole GPR tomography is identical in principle to seismic tomography. A transmitter antenna, moved to numerous locations in one borehole, radiates high-frequency EM pulses that are recorded by a receiver antenna, which is moved down a second borehole. Most commonly, inversion of the resulting data is accomplished by assuming that the propagating radar energy can be modelled by infinite-frequency rays that join the centres of the antennas. Under this assumption, first-break traveltimes and amplitudes of the data can be used to determine the distribution of subsurface EM-wave velocity and attenuation. The resulting ray-based tomographic images of the subsurface, however, are limited in resolution to approximately the width of the first Fresnel zone associated with the propagating pulse bandwidth (Williamson and Worthington, 1993). In order to improve resolution, we require modelling algorithms that account for more detailed physical aspects of the crosshole GPR experiment, such as wave propagation and antenna behaviour. These algorithms can be employed in waveform-based inversion strategies that use all of the recorded data to determine subsurface properties (e.g., Pratt and Worthington, 1988; Zhou et al., 1995).

There are a number of approaches to crosshole GPR modelling. None of these, however, allow for the simulation of both antenna transmission and reception in heterogeneous media. Sato and Thierbach (1991), for example, analytically modelled a crosshole GPR experiment using an expression for the current on an insulated dipole antenna derived by King and Smith (1981). Although their approach gives much insight into the effects of antenna and system parameters on recorded GPR wavelets, it requires a homogeneous medium between the boreholes and that the antennas are each in the far field of the other. In addition, the expression used for the antenna current is invalid for the case of water-filled boreholes and is thus only suitable for modelling in the vadose zone. Holliger and Bergmann (2002), on the other hand, numerically modelled crosshole GPR using a FDTD approach in 2D cylindrical coordinates. In their formulation, only the transmitter borehole was included in the model, and the antennas were simulated as point vertical electric dipoles. Ernst et al. (2006) further developed this algorithm to allow for detailed modelling of a realistic, finite-length transmitter antenna. Ellefsen and Wright (2005) employed a similar approach to examine the radiation patterns of realistic borehole GPR antennas. With these methods, much can be learned about the effects of the borehole, subsurface heterogeneity, and antenna characteristics on crosshole GPR radiation.

We present an algorithm to efficiently simulate crosshole GPR transmission in heterogeneous media. This is accomplished using FDTD modelling in 2D cylindrical coordinates. The algorithm can be easily implemented using a perfectly matched layer (PML) for absorbing boundaries, frequency-dependent media, and a finite-length transmitter antenna. The approach allows us to systematically explore the effects of various complicating factors on the radiated GPR signals. In this chapter, we examine waveguide effects due to the existence of a water-filled borehole, and show that guided waves are affected by the diameter of the borehole, the length of the antenna and the shape of transmitting signal.

3.2. FDTD in Cartesian coordinates

We start with the following Maxwell's equations

$$\frac{\partial \mathbf{D}}{\partial t} = \nabla \times \mathbf{H},$$ (3.1)

$$\mathbf{D}(\omega) = \varepsilon_0 \cdot \varepsilon_r^*(\omega) \cdot \mathbf{E}(\omega),$$ (3.2)

$$\frac{\partial \mathbf{H}}{\partial t} = -\frac{1}{\mu_0} \nabla \times \mathbf{E},$$ (3.3)

where $\mathbf{D}$ (C/m^2) is the electric flux density, $\mathbf{E}$ (V/m) is the electric field, $\mathbf{H}$ (A/m) is the magnetic field, ω (Hz) is the angular frequency, ε_0 (= 8.854 × 10^{-12} F/m) and μ_0 (= 4π × 10^{-7} H/m) are dielectric permittivity and magnetic permeability in free space, respectively, and

$$\varepsilon_r^*(\omega) = \varepsilon_r + \frac{\sigma}{j\omega\varepsilon_0},$$ (3.4)

where ε_r is the relative dielectric constant, and σ (S/m) is the conductivity. In this formulation, it is assumed that the materials being simulated are nonmagnetic; that is $\mathbf{H} = \mathbf{B}/\mu_0$, where $\mathbf{B}$ (Wb/m^2) is the magnetic induction. There is a reason for using this formulation; equations (3.1) and (3.3) remain the same regardless of the material, and any complicated mathematics stemming from the material is in equation (3.2). The solution of equation (3.2) can be viewed as a digital filtering problem (Sullivan, 2000), and the simulation of frequency-dependent media, for example, can be easily addressed.

We further normalize Maxwell's equations by substituting

$$\tilde{\mathbf{E}} = \sqrt{\frac{\varepsilon_0}{\mu_0}} \mathbf{E} \approx \frac{\mathbf{E}}{120\pi},$$ (3.5)

$$\tilde{\mathbf{D}} = \frac{\mathbf{D}}{\sqrt{\varepsilon_0 \mu_0}} = c_0 \mathbf{D} \,, \tag{3.6}$$

where c_0 (m/s) is the speed of light. This is the system of Gaussian units. The reason for using it is simplicity in the formulation. The electric and magnetic fields have the same order of magnitude. This has an advantage in formulating PML, which is a crucial part of FDTD simulation (Appendix 1).

We will drop the ~ notation, but it will always be assumed that we are referring to the normalized values. Equations (3.1) and (3.3) produce six scalar equations

$$\frac{\partial D_x}{\partial t} = c_0 \left(\frac{\partial H_z}{\partial y} - \frac{\partial H_y}{\partial z} \right), \tag{3.7}$$

$$\frac{\partial D_y}{\partial t} = c_0 \left(\frac{\partial H_x}{\partial z} - \frac{\partial H_z}{\partial x} \right), \tag{3.8}$$

$$\frac{\partial D_z}{\partial t} = c_0 \left(\frac{\partial H_y}{\partial x} - \frac{\partial H_x}{\partial y} \right), \tag{3.9}$$

$$D(\omega) = \varepsilon_r^* \cdot E(\omega), \tag{3.10}$$

$$\frac{\partial H_x}{\partial t} = -c_0 \left(\frac{\partial E_z}{\partial y} - \frac{\partial E_y}{\partial z} \right), \tag{3.11}$$

$$\frac{\partial H_y}{\partial t} = -c_0 \left(\frac{\partial E_x}{\partial z} - \frac{\partial E_z}{\partial x} \right), \tag{3.12}$$

$$\frac{\partial H_z}{\partial t} = -c_0 \left(\frac{\partial E_y}{\partial x} - \frac{\partial E_x}{\partial y} \right). \tag{3.13}$$

The original FDTD paradigm was described by the Yee cell in Fig. 3.1 (Yee, 1966). The E and H fields are assumed interleaved around a cell whose origin is at the location (i, j, k). Every E field is located 1/2 cell width from the origin in the direction of its orientation; every H field is offset 1/2 cell in each direction except that of its orientation.
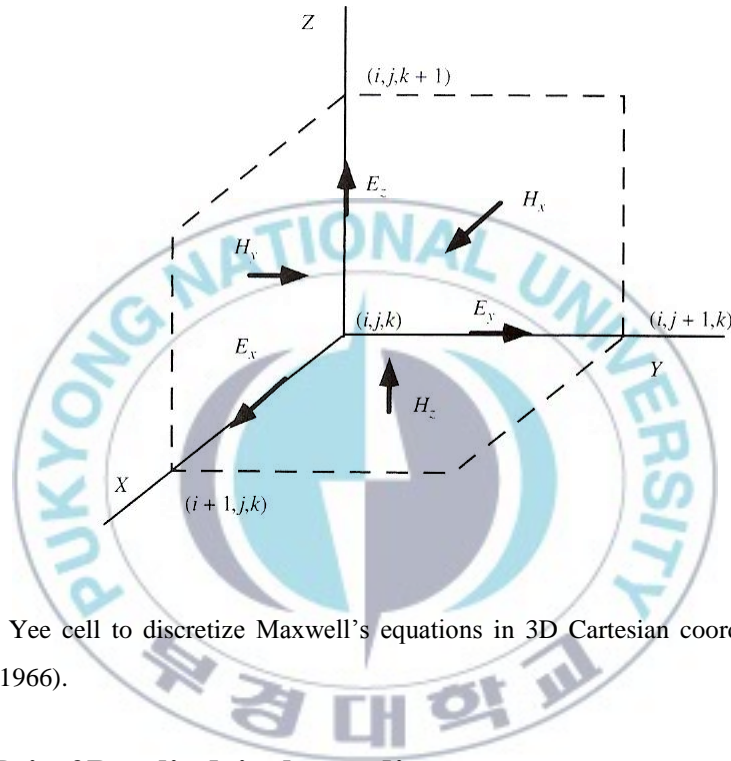
Fig. 3.1. The Yee cell to discretize Maxwell's equations in 3D Cartesian coordinates (After Yee, 1966).

3.3. FDTD in 2D cylindrical coordinates

The core of our modeling approach is the FDTD solution of Maxwell's equations in 2D cylindrical coordinates. In this formulation, rotational symmetry about the vertical z-axis is assumed so that Maxwell's equations can be separated into the transverse electric (TE) and transverse magnetic (TM) modes, which are two sets of coupled partial-differential equations involving the (E_ϕ, H_ρ, H_z) and (E_ρ, E_z, H_ϕ) components, required. Dropping the ~ notation

$$\frac{\partial D_\phi}{\partial t} = c_0 \left(\frac{\partial H_\rho}{\partial z} - \frac{\partial H_z}{\partial \rho} \right), \qquad (3.14)$$

$$D(\omega) = \varepsilon_r^* \cdot E(\omega), \qquad (3.15)$$

$$\frac{\partial H_\rho}{\partial t} = c_0 \left(\frac{\partial E_\phi}{\partial z} \right), \qquad (3.16)$$

$$\frac{\partial H_z}{\partial t} = c_0 \left[\frac{1}{\rho} \frac{\partial(\rho E_\phi)}{\partial \rho} \right], \qquad (3.17)$$

and

$$\frac{\partial D_\rho}{\partial t} = -c_0 \frac{\partial H_\phi}{\partial z}, \qquad (3.18)$$

$$\frac{\partial D_z}{\partial t} = c_0 \left[\frac{1}{\rho} \frac{\partial(\rho H_\phi)}{\partial \rho} \right], \qquad (3.19)$$

$$D(\omega) = \varepsilon_r^* \cdot E(\omega), \qquad (3.20)$$

$$\frac{\partial H_\phi}{\partial t} = c_0 \left(\frac{\partial E_z}{\partial \rho} - \frac{\partial E_\rho}{\partial z} \right). \qquad (3.21)$$

Equations (3.14) – (3.17) are the TE mode, while equations (3.18) – (3.21) the TM mode. For crosshole GPR modeling where the antennas are oriented parallel to the z-axis, only the TM mode equations are required.

These equations are solved numerically in the time domain using a leap-frog, staggered-grid approach in the time domain, which involves offsetting the electric- and magnetic-field components so that the FD approximations of all partial derivatives are centered in both space and time (Yee, 1966). Stepping forward in time is accomplished by alternately updating the electric and magnetic fields. All updates are explicit.

We locate our field components in space identically to Holliger and Bergmann (2002) to avoid singularity problems associated with equation (3.14) on the z-axis as shown in Fig. 3.2; there is no E_z component located at $\rho = 0$. Fig. 3.2 also shows the allocation of electric- and magnetic-field components on each cell; the electric- and magnetic-field components are located at the edges and the center of a cell,

respectively. Because the electric fields are set to cell edges, an averaged conductivity and permittivity must be evaluated at the edges (Appendix 2).

We choose the time step Δt according to the Courant numerical stability criterion

$$\Delta t \leq \frac{1}{c_{max} \sqrt{(1/\Delta\rho)^2 + (1/\Delta z)^2}} \, , \qquad (3.22)$$

where $\Delta\rho$ and Δz are the discretization sizes along the ρ and z axes, respectively, and $c_{max} = 1/(\varepsilon_{min}\mu_0)^{1/2}$ is the maximum phase velocity in the FD grid, with ε_{min} being the lowest value of the dielectric permittivity.

We also use second-order-accurate FD approximations for all derivatives, which mean that 10 grid-points per minimum wavelength are needed to control
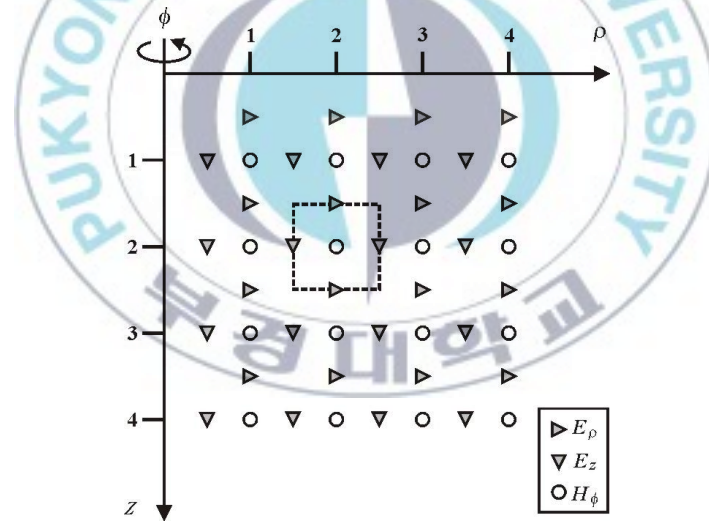
Fig. 3.2. The staggered FD grid used to discretize Maxwell's equations in 2D cylindrical coordinates (after Holliger and Bergmann, 2002). The electric- and magnetic-field components are located at the edges and the centre of a cell such as that denoted by dotted lines.

numerical dispersion. Higher-order approximations can be used for the spatial and/or temporal derivatives in our code, with a moderate increase in code complexity, in order to decrease the needed number of field points and thus reduce computing time (e.g., Bergmann et al., 1999).

3.4. Validation

For numerical simulations we use a FD grid consisting of 510×1200 cells and uniform cell width of $\Delta\rho = \Delta z = 1$ cm. PML absorbing boundaries were implemented in cylindrical coordinates to prevent reflections from the top, bottom, and right-hand sides of the simulation grid (Berenger, 1994; Sullivan, 2000). A model consist of a homogeneous medium ($\varepsilon = 9\varepsilon_0$, $\sigma = 1$ mS/m) containing air-filled borehole ($\varepsilon = \varepsilon_0$, $\sigma = 0$ S/m).

With the cylindrical symmetry, the transmitter antenna and its borehole, which are centered on the z-axis, can be explicitly and accurately represented with the above approach. In this study, a dipole antenna is used as the transmitter antenna. It consists of two metal arms. A dipole antenna functions by having current run through the arms, which results in radiation. FDTD simulates a dipole antenna in the following way: The metal of the arms is specified by setting its E_z field as zero, which insures its conductivity be infinite in the corresponding metal cells. The source is specified by setting the E_z field in the gap, the cell in between the two arms, to a certain value. For simplicity, we specify a Gaussian voltage pulse $V(t)$ as (Sullivan, 2000; Ellefsen and Wright, 2005)

$$V(t) = \exp\left[-\frac{(t - t_0)^2}{2\tau^2}\right], \tag{3.23}$$

where τ is a pulse width, and t_0 is an appropriate time shift to ensure causality to define the source field

$$E_z(t) = -V(t) / \Delta z, \tag{3.24}$$

at the gap. In this chapter, we assign $t_0 = 33.3$ ns and $\tau = 4$ ns, except for the last case examining the pulse width on waveguide effects. With these values, the source voltages are significant between 18 ns and 51 ns (Fig. 3.3a). In the frequency domain, the amplitude decreases gradually as the frequency increases (Fig. 3.3b). The received signal was represented by the electric field at the observation point.

We examine our 3D FDTD modeling for a simple model, which consist of a homogeneous medium ($\varepsilon = 9\varepsilon_0$, $\sigma = 1$ mS/m) containing water-filled borehole ($\varepsilon = 80\varepsilon_0$, $\sigma = 1$ mS/m). A 3D FD grid consists of $510 \times 120 \times 120$ cells and uniform cell width of $\Delta x = \Delta y = \Delta z = 10$ cm. PML absorbing boundaries were implemented in Cartesian coordinates to prevent reflections from the top, bottom, and, right- and left-hand sides of the simulation grid (Berenger, 1994; Sullivan, 2000). A source applied to the transmitter is a Gaussian voltage pulse with a pulse width of 4 ns. Fig. 3.4 compares E_z fields calculated by 3D and 2D FDTD schemes, respectively. Reflected waves are clearly show in a portion of the wave propagates into the cavity in both figures, similarly.

Fig. 3.5 shows snapshots of E_z fields initiated from a 20 cm dipole antenna in an air-filled borehole having a diameter of 9 cm. As the wave reaches PML, which is
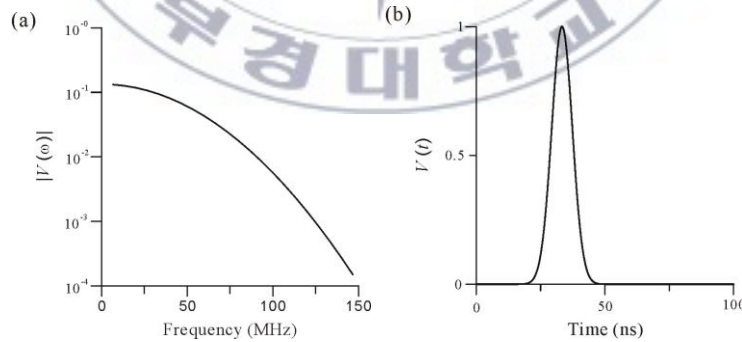
Fig. 3.3. Voltage used for FDTD simulations (a), and power spectrum of the voltage (b). The spectrum is normalized by its maximum value.
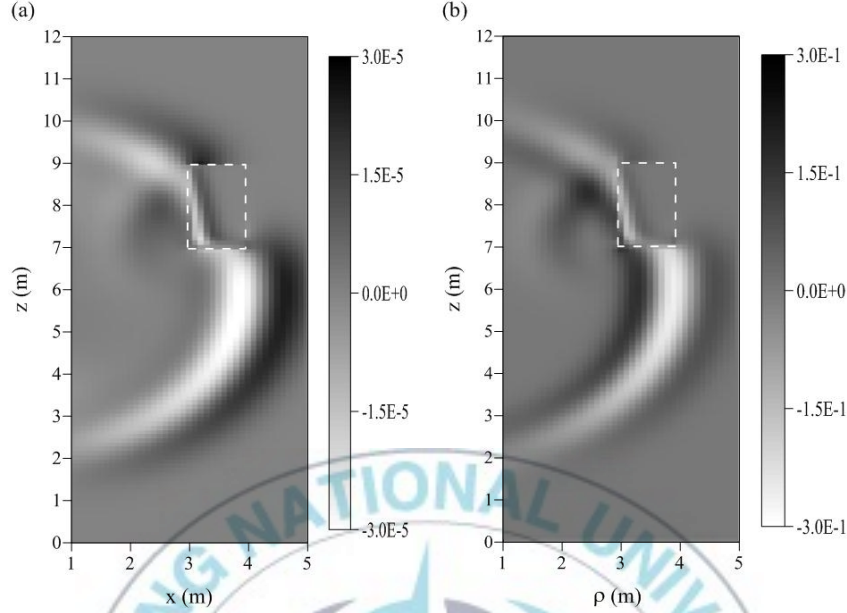
Fig. 3.4. Snapshots of E_z fields at 80 ns for model with water-filled cavities, calculated from 3D FDTD modeling (a) and 2D FDTD modeling (b), respectively. The outgoing wave, initiated from a 20 cm dipole antenna located at $z = 6$ m, moves slower inside the water-filled cavities which are 1 m × 2 m in size (dotted rectangles).

eight cells thick on top, bottom, and right-hand sides, it is absorbed. The effectiveness of PML is apparent in the right figure, because the image would not be concentric circles if the outgoing wave partially reflected.

Fig. 3.6 compares E_z fields for models with air- and water-filled ($\varepsilon = 80\varepsilon_0$, $\sigma = 1$ S/m) cavities, which are 1 m × 1.5 m in size. The outgoing wave, generated from a 20 cm dipole antenna located at $z = 6$ m in an air-filled borehole having a diameter of 9 cm, moves about three times faster and slower in the air-and water-filled cavities, respectively, than in the homogeneous background. Note that a portion of the wave propagates into the cavity and a portion is reflected, in keeping with basic EM theory.
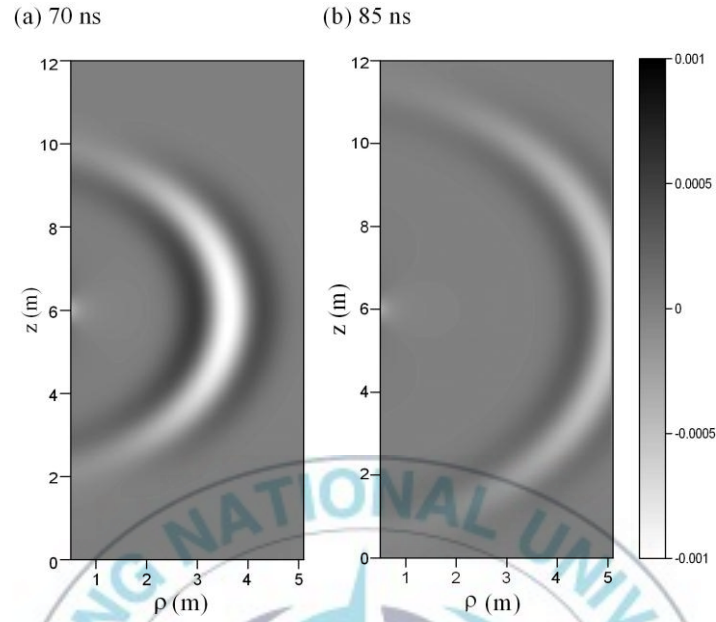
Fig. 3.5. Snapshots of E_z fields at 70 ns (a) and 85 ns (b) for a homogeneous model. Outgoing waves, generated from a 20 cm dipole antenna at z = 6 m in an air-filled borehole having a diameter of 9 cm, remain concentric. Only when the wave gets within eight points of the top, bottom, and right-hand edges, which are inside PML, does distortion start to occur.
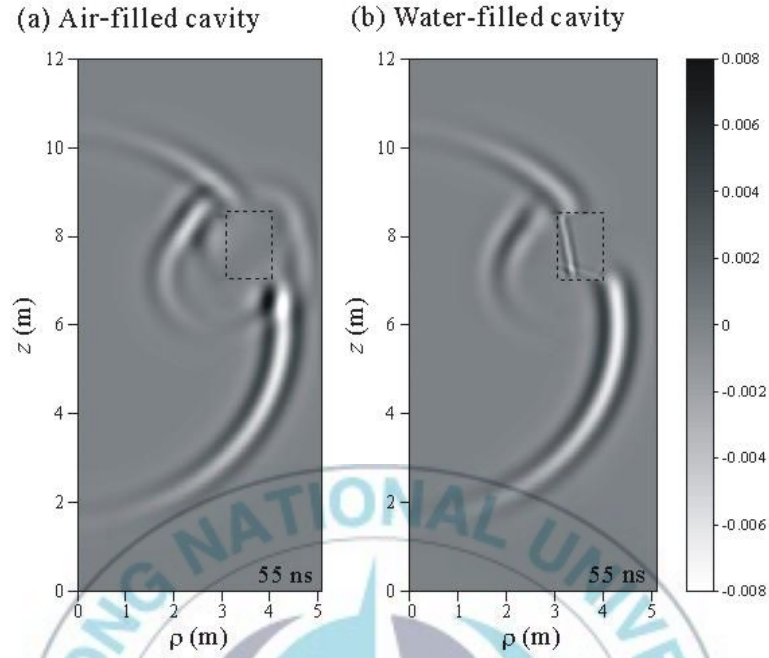
Fig. 3.6. Snapshots of E_z fields at 55 ns for models with air-filled (a) and water-filled (b) cavities, denoted by dotted rectangles which are 1 m × 1.5 m in size. The outgoing wave, initiated from a 20 cm dipole antenna located at $z = 6$ m in an air-filled borehole having a diameter of 9 cm, moves faster and slower inside the air-filled and water-filled cavities, respectively. Many reflections are generated at the cavity boundaries.

3.5. Waveguide effects

Waveguide phenomenon due to a borehole is often observed in borehole radar measurements. The phenomenon deforms the antenna pattern and can cause artifacts in radar measurements (Ebihara et al., 1998). In this chapter, we consider the radiation pattern of antenna, which are located in water-filled borehole, specially. As Holliger and Bergmann (2002) pointed out, resonance effects due to a dry borehole should not be significant provided that the EM-wave velocity in the borehole is faster than in the embedding medium. The situation is, however, completely different in the presence of a water-filled borehole. The dielectric constant of water is much higher than that of the surrounding material and thus water in a borehole functions as a waveguide for EM waves. The mechanism of the waveguide is similar to the 'tube wave' in borehole seismic. The guided wave is a wave for a cylindrical interface between the two media. In this regard, the numerical scheme explained previous chapter is suitable for modeling waveguide effects. The waveguide effects highly depend on the length of the transmitter antenna, the medium filling the borehole, and the diameter of the borehole.

3.5.1. Effect of borehole filling materials

To implement numerical simulation of waveguide effect with variation of filling material of the borehole, we use the same FD grid and source with previous examples. Our analyses are based on the same canonical models as used in Holliger and Bergmann (2002): a homogeneous medium ($\varepsilon = 9\varepsilon_0$, $\sigma = 1$ mS/m) containing air-filled borehole ($\varepsilon = \varepsilon_0$, $\sigma = 0$ S/m) or water-filled borehole ($\varepsilon = 80\varepsilon_0$, $\sigma = 1$ mS/m).

Fig. 3.7 shows transmitted pulses and their amplitude spectra. The EM wavefields are generated from a 20 cm dipole antenna located in the center of source borehole with a diameter of 9 cm and observed at a point of 5 m horizontally away from the source antenna. In the illustrations, the EM waveforms and the spectra are normalized by the maximum amplitude of first-cycle direct wave and by that of source signal shown in Fig. 3.8, respectively.

A reverberatory character can be found after the first cycle of the pulse only in the case of water-filled borehole. This is because the water-filled borehole acts as a waveguide. The amplitude of the reverberation becomes smaller with time. An air-filled borehole produces no clear reverberation and the waveform has the shape of Ricker wavelet. This is the same feature as the case for a homogeneous reference model without borehole. Furthermore, the shapes of radiated waves are essentially indistinguishable in between the cases of air-filled borehole and a homogeneous full-space. Also, the spectrum shapes for the two models are similar to each other. The water-filled borehole, however, produces a peak spectrum at about 85 MHz.
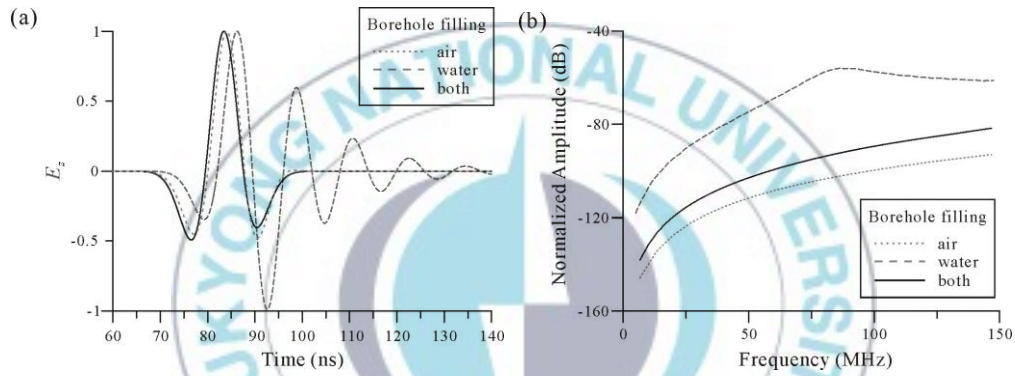
Fig. 3.7. Normalized vertical electric fields (a) and their power spectra (b) at a point of 5 m from the center of a 20 cm transmitter antenna located in air- and water-filled boreholes with a diameter of 9 cm.

3.5.2. Effect of borehole diameters

In the water-filled borehole, the change of borehole diameters can effect on guided wave. Fig. 3.8 compares normalized E_z fields measured at 5 m from the boreholes with various diameters: 7, 9, 11 and 13 cm. A clear reverberatory character can be found after the direct wave (Fig. 3.8a). The reverberations gradually decay with time. Furthermore, the pulse length of the reverberations becomes longer as the increase of

- 27 -

the borehole diameter. The borehole effect on the reverberations is also recognized in the frequency domain (Fig. 3.8b). The water-filled borehole produces peak amplitudes at about 80 MHz in the spectrum, and the peak is shifted to lower frequencies to approach to the resonance frequency of 67 MHz in water as the borehole diameter increases. These finding implies that borehole measurements may be optimized by the observation frequency taking into account the borehole diameter if the borehole is filled with water.

Fig. 3.8. Normalized vertical electric fields (a) and their power spectra (b) at a point of 5 m from the center of a 20 cm transmitter antenna located in a water-filled borehole with diameters of 7, 9, 11 and 13 cm.

Fig. 3.9 compares the normalized maximum first-cycle amplitudes of synthetic wavefields along a vertical line at a distance of 5 m from the symmetric axis for the models containing water-filled boreholes with the amplitudes for a model having an air-filled borehole. The radius of the air-filled borehole has little effect on the normalized amplitude compared with the radius effect for the reference model. In contrast, water-filled boreholes can distort the amplitude radiation, and the resulting amplitudes increase with the radius of the water-filled borehole.

- 28 -
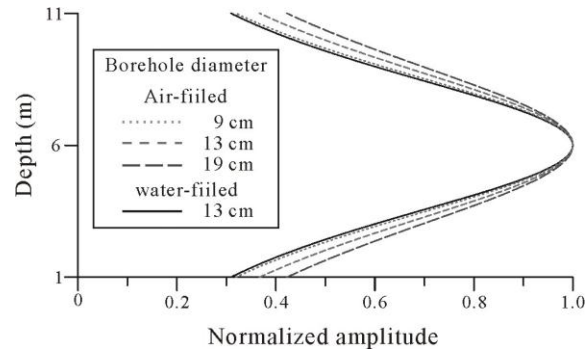
Fig. 3.9. Normalized maximum first-cycle amplitudes observed along a vertical line at a distance of 5 m from the center of a 20 cm transmitter antenna located in air- (solid) and water-filled (dashed) boreholes. The diameters of air- and water-filled boreholes are set to 9, 13 and 19 cm, respectively.
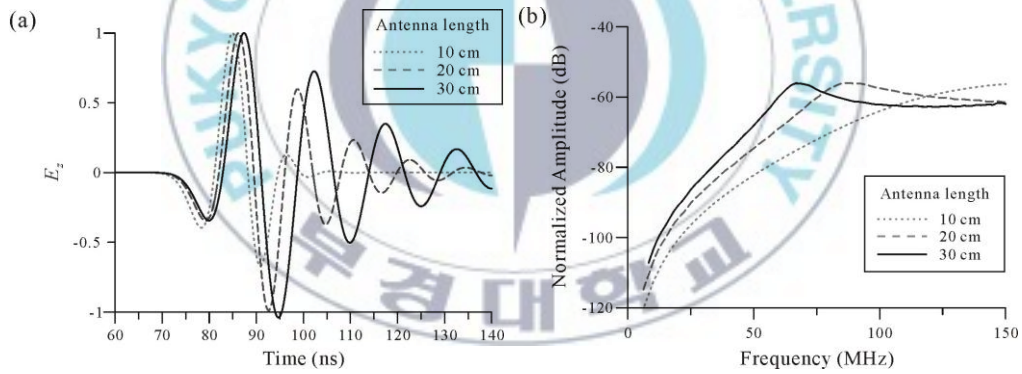
Fig. 3.10. Normalized vertical electric fields (a) and their power spectra (b) at a point of 5 m from the center of a water-filled borehole with a diameter of 9 cm. The transmitted pulses are generated from dipole antennas of 10, 20 and 30 cm long in the borehole.

3.5.3. Effect of antenna lengths

Antennas of different lengths are simulated in order to examine the effect of antenna length on the waveguide effect of water-filled borehole. Fig. 3.10 compares transmitted pulses and their spectra generated from 10, 20 and 30cm long antennas located in a
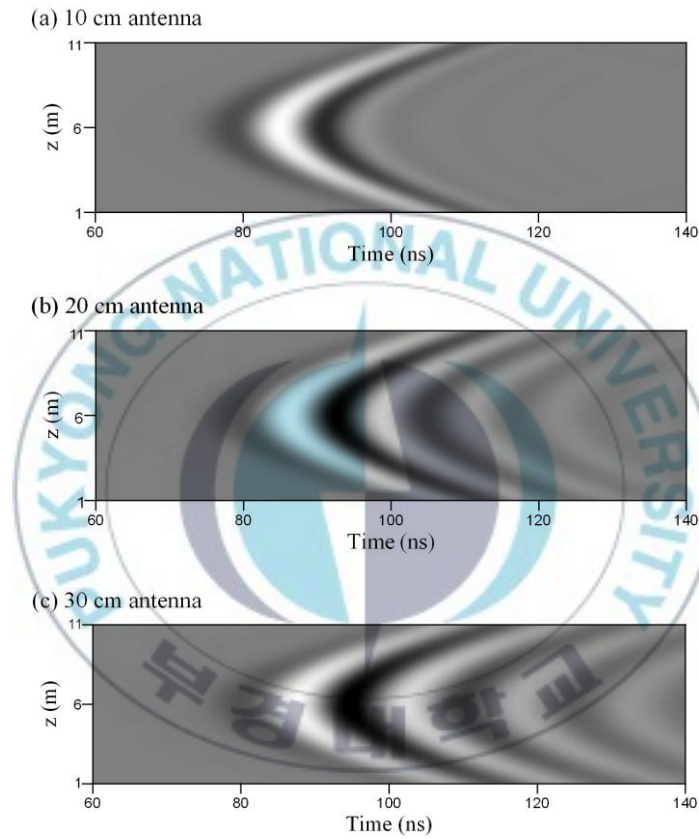
Fig. 3.11. Radargrams consisting of the E_z-component of the EM wavefield radiated from a transmitter antenna located in a water-filled borehole with a diameter of 9 cm. Three antenna lengths are considered: 10 (a), 20 (b) and 30 cm (c). The data are collected along a vertical line at a distance of 5 m from the symmetry axis.

water-filled borehole with a diameter of 9 cm, and Fig. 3.11 shows radargrams collected along a vertical line at a distance of 5 m from the symmetric axis of the borehole. The longer the length of the transmitter antenna, the more pronounced the reverberatory character. Note that the 10 cm long antenna generates little reverberation.

3.5.4. Effect of pulse widths

To confirm the effect of pulse width on antenna radiation pattern, three pulse widths of $\tau = 4$, 5 and 6 (ns) are considered. Fig. 3.12 illustrates the effect of the pulse width of the source signal on radiated wavefields. The resulting radiated waves are collected at a point of 5 m from the center of a 20 cm antenna located in a water-filled borehole with a diameter of 9 cm. The source pulse width highly affects the amplitude variations of the resulting guided waves. The amplitudes of reverberated waves decay more rapidly as the pulse width increases.
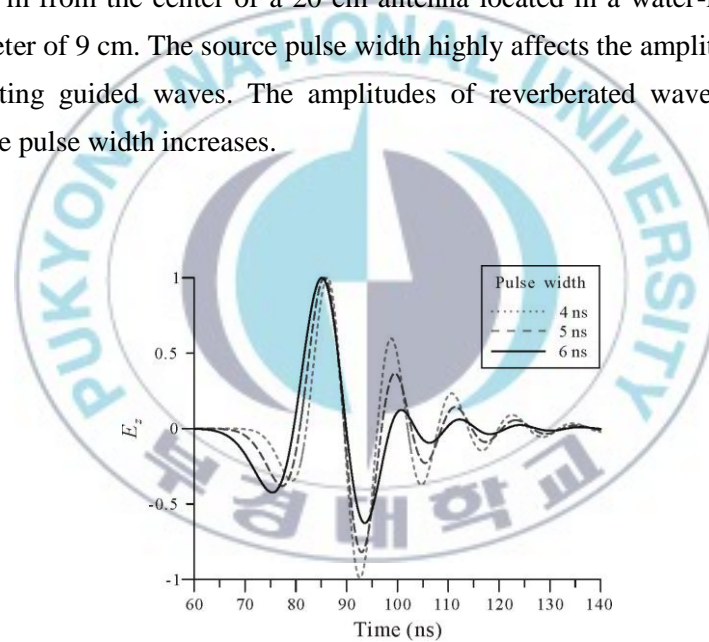
Fig. 3.12. Normalized vertical electric fields at a point of 5 m from the center of a 20 cm transmitter antenna located in a water-filled borehole with a diameter of 9 cm. Three pulse widths are considered: $\tau = 4$, 5 and 6 ns.

3.5.5. Effect of water levels

We have assumed that the source borehole was filled with a homogeneous material: air or water. In crosshole surveys, however, we frequently observe a water table. When an electric dipole antenna is located near the water level, radiated energy becomes coupled to the interface and the resulting radiation pattern may be different from the homogeneous case. In this section, we consider a model of borehole which is filled with both air and water. The water table is located at 1 cm below, 1 cm above, 5 cm above, and 10 cm above the feeding point of the source antenna (Fig. 3.13). Fig. 3.14 compares normalized E_z fields measured at 5 m from the boreholes with the various antenna positions. When the antenna feeding point is in the air (Fig. 3.13a), reverberatory character cannot be found after the first-cycle amplitude. However, the more the antenna goes down into the water, the more the reverberations are strong (Figs. 3.13b ~ d).
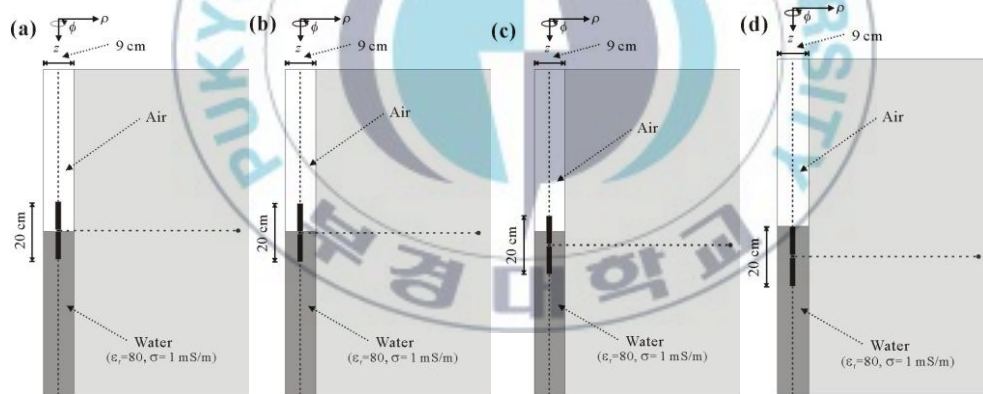
Fig. 3.13. Schematic models showing four water levels in the source borehole. The center of transmitting antenna is moved down from the water level to the 10 cm below the level.
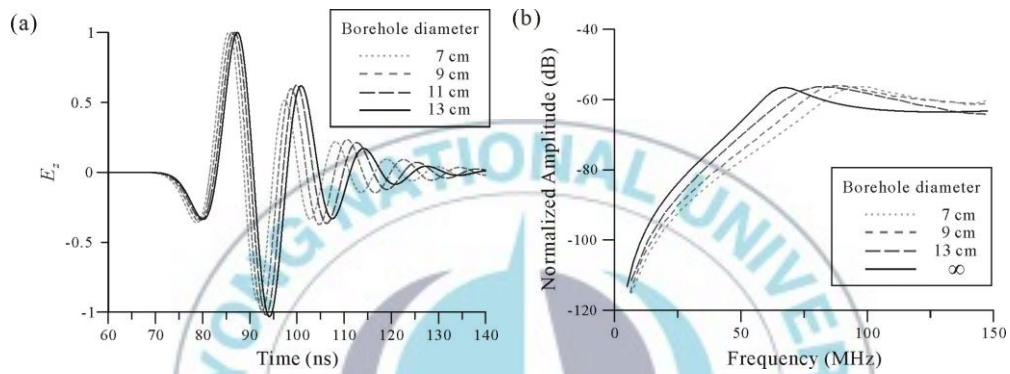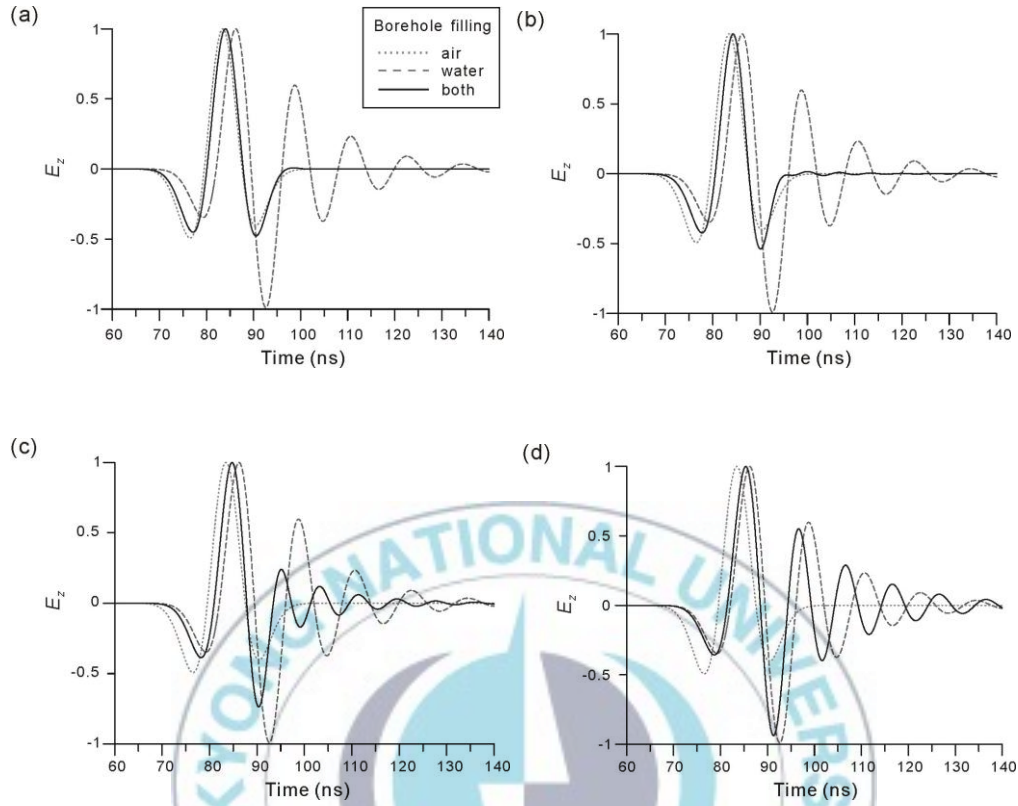
Fig. 3.14. Normalized vertical electric fields at a point of 5 m from the center of a 20 cm transmitter antenna located in both air- and water-filled borehole. The center of transmitting antenna is in the air (1 cm above the water level (a)), and in the water (1 (b), 5 (c) and 10 cm (d) below the level).

When the center of transmitting antenna is located at 1 cm below or above the water level, the spectrum shape is nearly similar with that of air-filled borehole. The power spectrum shows a clear peak, and the peak amplitude is shifted to 100 MHz with the antenna depth below the water level (Fig. 3.15). From these results, we can find the waveguide effects highly depend on the water level.
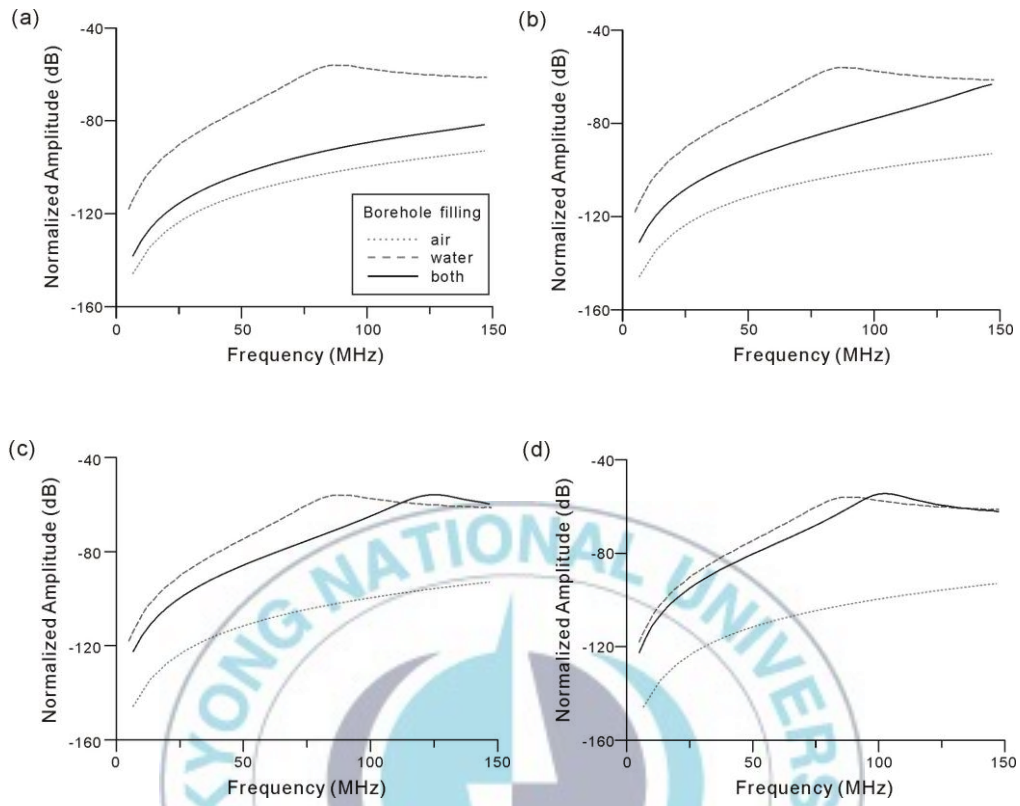
Fig. 3.15. Power spectra of normalized vertical electric fields at a point of 5 m from the center of a 20 cm transmitter antenna located in both air- and water-filled borehole. The center of transmitting antenna is in the air (1 cm above the water level (a)), and in the water 1 (b), 5 (c) and 10 cm (d) below the level.

3.6. Summary

We have presented a FD solution of Maxwell's equations in cylindrical coordinates which is suitable for modelling crosshole GPR data. This algorithm was used to model the EM wavefield radiated from a vertical electric antenna located in a borehole filled with air or water. Major simplifications made in this study were that only the radiation pattern of the transmitter was accounted for explicitly and that the received signal was represented by the electric field at the observation point. The radiation pattern of an antenna located in a water-filled borehole is severely distorted by a waveguide effect that depends on the length of the transmitter antenna, the medium filling the borehole, and the diameter of the borehole. Given that most shallow boreholes are at least partially water-filled, this has potentially serious implications for the interpretation of crosshole GPR data. Further complications of the radiation pattern, regardless of the medium filling the borehole, must be expected to arise from vertical stratification and lateral heterogeneity of electric parameters in the shallow subsurface.

Appendix 1

Without the proper truncation of the problem space by appropriate boundary conditions, unwanted reflections would return to cause errors in the simulation (Fig. A1.1). These outgoing waves must be eliminated by an absorbing boundary condition (ABC).
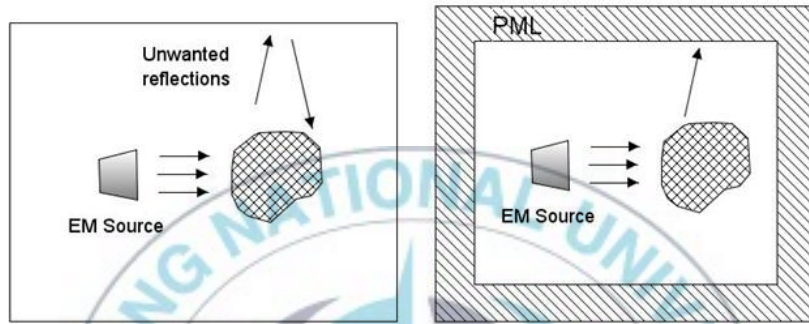
Fig. A1.1. Without an absorbing boundary condition, outgoing waves are reflected back into the problem space (left). Reflected outgoing waves are truncated with the perfectly matched layer (right) (After Sullivan 2000).

One of the most flexible and efficient ABCs is the PML developed by Berenger (1994). The basic idea as follows: If a wave is propagating in one medium and it impinges upon another medium, the amount of reflection (Γ) is dictated by the intrinsic impedances (η) of the two media (Fig. A1.2)

$$\Gamma = \frac{\eta_A - \eta_B}{\eta_A + \eta_B},$$
(A1.1)

where η is determined by the dielectric constants (ε) and permeabilities (μ) of the two media
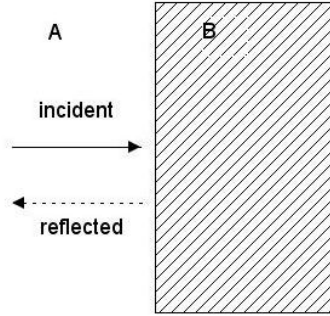
Fig. A1.2. The reflection at the interface of two media is dependent on their respective impedances (After Sullivan 2000).

$$\eta = \sqrt{\frac{\mu}{\varepsilon}} \ . \tag{A1.2}$$

Normally, in free space, $\varepsilon = \varepsilon_0$ and $\mu = \mu_0$, but in our normalized units, $\eta = 1$ in free space. When we added the flux density formulation, we switched to

$$\varepsilon_F \frac{\partial \mathbf{E}}{\partial t} = \nabla \times \mathbf{H} \ , \tag{A1.3}$$

$$\mathbf{D}(\omega) = \varepsilon^*(\omega) \cdot \mathbf{E}(\omega), \tag{A1.4}$$

$$\mu_F \frac{\partial \mathbf{H}}{\partial t} = -\nabla \times \mathbf{E} \ . \tag{A1.5}$$

We have added fictitious dielectric constant and permeability, ε_F and μ_F, that we will use to implement the PML.

Sacks et al. (1995) shows that there are two conditions to form a PML:

1. The impedance going from the background medium to the PML must be constant,

$$\eta_0 = \eta_m = \sqrt{\frac{\mu^*_{Fx}}{\varepsilon^*_{Fx}}} = 1 \ . \tag{A1.6}$$

- 37 -

The impedance is unity because of our normalized units.

2. In the direction perpendicular to the boundary (the x direction, for instance), the relative dielectric constant and relative permeability must be the inverse of those in the other directions, i.e.,

$$\varepsilon^*{}_{Fx} = \frac{1}{\varepsilon^*{}_{Fx}}, \tag{A1.7}$$

$$\mu^*{}_{Fx} = \frac{1}{\mu^*{}_{Fx}}. \tag{A1.8}$$

We assume that each of these is a complex quantity of the form

$$\varepsilon^*{}_{Fm} = \varepsilon_{Fm} + \frac{\sigma_{Dm}}{j\varpi\varepsilon_0}, \qquad \text{for } m = x \text{ or } y, \tag{A1.9}$$

$$\mu^*{}_{Fx} = \mu_{Fx} + \frac{\sigma_{Hm}}{j\varpi\mu_0}, \qquad \text{for } m = x \text{ or } y. \tag{A1.10}$$

The following selection of parameters satisfies equations (A1.9) and (A1.10):

$$\varepsilon_{Fm} = \mu_{Fm} = 1, \tag{A1.11}$$

$$\frac{\sigma_{Dm}}{\varepsilon_0} = \frac{\sigma_{Hm}}{\mu_0} = \frac{\sigma_D}{\varepsilon_0}. \tag{A1.12}$$

Substituting equations (A1.11) and (A1.12) into (A1.9) and (A1.10), equation (A1.6) becomes

$$\eta_0 = \eta_m = \sqrt{\frac{\mu^*{}_{Fx}}{\varepsilon^*{}_{Fx}}} = \sqrt{\frac{1 + \sigma(x)/j\varpi\varepsilon_0}{1 + \sigma(x)/j\varpi\varepsilon_0}} = 1. \tag{A1.13}$$

- 38 -

This fulfills the first requirement above. If σ increases gradually as it goes into the PML, **D** and **H** are attenuated.

Appendix 2

The Ampere's law states relationship between magnetic field components along a closed elemental contour C bounding the corresponding open element surface S with the electric field distribution (Fig. A2.1), and

$$\oint_C \mathbf{H} \cdot d\mathbf{s} = \int_S \left(\varepsilon \frac{\partial \mathbf{E}}{\partial t} + \sigma \mathbf{E} \right) \cdot \mathbf{n} dS$$

$$= \left(\varepsilon_1 \frac{\partial E_z}{\partial t} + \sigma_1 E_z \right) \Delta x l_1 + \left(\varepsilon_2 \frac{\partial E_z}{\partial t} + \sigma_2 E_z \right) \Delta x l_2$$

$$= \left(\bar{\varepsilon} \frac{\partial E_z}{\partial t} + \bar{\sigma} E_z \right) \Delta x \Delta y , \qquad (A2.1)$$

where

$$\bar{\varepsilon} = \frac{\varepsilon_1 l_1 + \varepsilon_2 l_2}{\Delta y}, \text{ and } \bar{\sigma} = \frac{\sigma_1 l_1 + \sigma_2 l_2}{\Delta y} .$$

In particular, when $l_1 = l_2 = \Delta y/2$,

$$\bar{\varepsilon} = \frac{\varepsilon_1 + \varepsilon_2}{2}, \text{ and } \bar{\sigma} = \frac{\sigma_1 + \sigma_2}{2} . \qquad (A2.2)$$
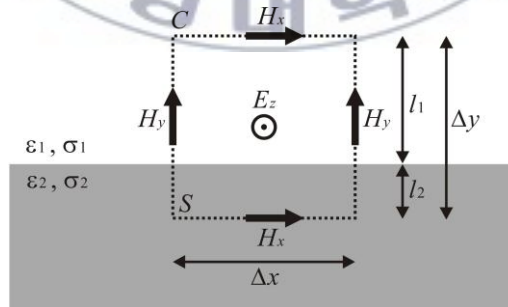
Fig. A2.1. Schematic representation of Ampere's integral expression near different two media.

Chapter 4. Slope analysis of radargrames

4.1. Introduction

An artificial groundwater recharge test was carried out in Nagaoka City, Japan (Kuroda et al., 2006). Time-lapse crosshole measurements were acquired to monitor the infiltration process in the vadose zone. Borehole GPR operated in ZOP mode was utilized to estimate water contents of soils using the dielectric constants derived from traveltimes of GPR pulses. Conventional ZOP data analysis, the EM wave velocity is calculated for a known antenna separation, assuming that the first-arriving energy travels along a direct path from the transmitter to the receiver. This assumption, however, can give rise to erroneous velocity estimates if refracted waves are first to arrive (Hammon et al., 2002; Huisman et al., 2003; Rucker and Ferré, 2003; 2004).

In this Chapter, we apply a method to determine the water content above the wetting front using the slope analysis of the traveltime versus depth profile. To simulate GPR wavefields and evaluate the dielectric permittivity accurately in the vadose zone, a FDTD solution of Maxwell's equations in 2D cylindrical coordinates is applied.

4.2. Cross-borehole radar simulation

Although the ZOP mode is rapid in data acquisition and straightforward in the processing and interpretation, multiple travel paths through the subsurface can give rise to measurement errors. Specifically, in layered media with sharp changes in water content with depth, critically refracted waves may arrive before direct waves at some depths. For the forward modeling of EM waves propagating in heterogeneous media, we employ a FDTD solution of Maxwell's equations in 2D cylindrical coordinates. The modeling scheme developed by Jang et al. (2007) is used to simulate EM fields radiated from a transmitter antenna located in a source borehole.

FDTD modeling in 2D cylindrical coordinates is applied to simulate radargrams. In modeling, we use a FD grid consisting of 370 × 600 cells, each of which is 1 cm by 1 cm, and specify a Gaussian voltage pulse $V(t)$. A Gaussian pulse with $t_0 = 6$ ns and $\tau = 2$ ns is applied. We consider first the effect of antenna lengths on the radiation pattern. A short antenna in an air-filled borehole produces no clear reverberations following the direct wave for a homogeneous model (Fig. 4.1). Fig. 4.1 compares transmitted pulses and their spectra radiated from 0.2 m and 1 m long transmitting antennas located in an air-filled borehole with a diameter of 7 cm. The long antenna generates a wavetrain (Fig. 4.6a) which comprises a pulse of EM waves with a frequency of about 100 MHz (Fig. 4.6b), whereas the short antenna radiates a simple pulse like a Ricker wavelet.
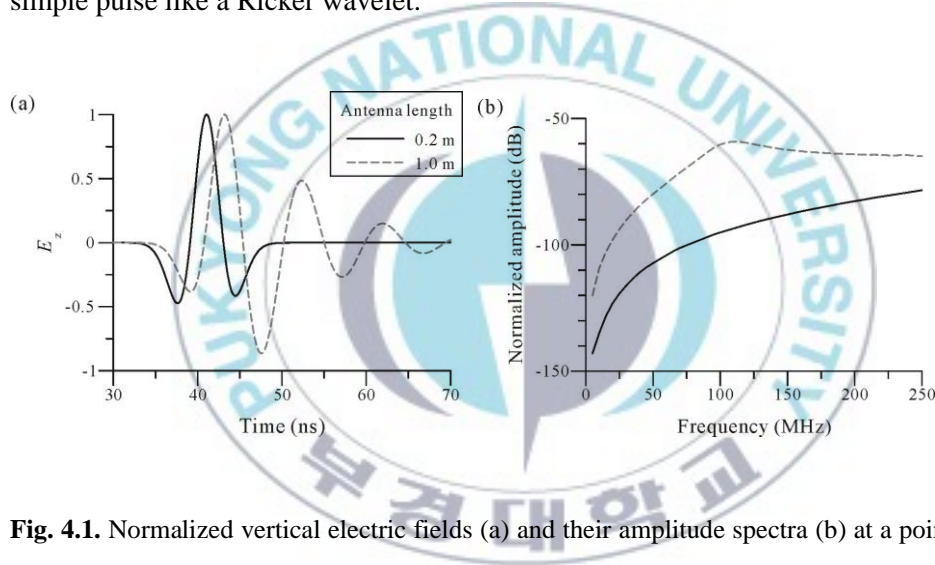
Fig. 4.1. Normalized vertical electric fields (a) and their amplitude spectra (b) at a point of 3.58 m from the center of an air-filled borehole with a diameter of 7 cm. The transmitted pulses are generated from dipole antennas of 0.2 m and 1.0 m long.

One of the most pronounced features in observed waveforms is reverberations following the first-cycle maximum amplitude as can be seen in Fig. 2.2. This phenomenon is commonly observed regardless of the degree of water saturation. Jang et al. (2007) showed that a short antenna in an air-filled borehole produces no clear reverberations following the direct wave for a homogeneous model. Fig. 4.1 compares

transmitted pulses and their spectra radiated from 0.2 m and 1 m long transmitting antennas located in an air-filled borehole with a diameter of 7 cm. The 1 m antenna generates a wavetrain (Fig. 4.1a) which comprises a pulse of EM waves with a frequency of about 100 MHz (Fig. 4.1b), whereas the 0.2 m antenna radiates a simple pulse like a Ricker wavelet. We have found that setting a Gaussian pulse with $t_0 = 6$ ns and $\tau = 2$ ns as a source yields a good approximation to the observed radargrams.

4.3. Slope analysis

The spatial and temporal distribution of water content was derived from velocity estimates based on the standard ZOP method that assumes that all first arrivals are direct. However, critical refractions can occur whenever EM waves traveling through a low-velocity medium reaches a boundary with a higher-velocity medium. If the GPR antennas are located within a high water content layer that is adjacent to a lower water content layer, critically refracted waves may arrive before direct waves. Although critical refractions cannot be distinguished from direct arrivals on a single radargram, they exhibit identifiable behavior on a traveltime profile. The traveltime of a critically refracted wave can be shorter than that of a direct wave if the measurement is taken close to the boundary between two layers of contrasting dielectric permittivity (Hammon et al., 2002; Huisman et al., 2003; Rucker and Ferré, 2003; 2004).

In the intermediate state of about 52 min after infiltration (Fig. 2.2b), the first arrival traveltime increased significantly at depths shallower than 4.0 m compared with the initial state (Fig. 2.2a), clearly indicating an increase of water content. The first arrival time of a critically refracted wave must decrease linearly with depth above the wetting front if the zone is composed of layered media with sharp changes in water content. Once the first arrival times are classified as direct or critically refracted, the dielectric constant and water content can be determined using equations (2.1) and (2.2).

Here we select a simple 1D layered model with thicker layers than that used in the standard ZOP method to avoid a hidden layer problem associated with the thinness of the layer (Reynolds, 1997). Three 0.4 m thick layers are selected in the top 4 m, and

thus three straight lines are fitted to the traveltime profile for critical refractions as shown in Fig. 4.2. Once the slopes of refracted arrivals are identified, refracting interfaces are easily determined (Rucker and Ferré, 2003; 2004). Fig. 4.3 compares the dielectric constant profile obtained from considering critical refractions with the profile assuming that all first arrivals are direct waves. Critical refractions are also considered below 4 m.
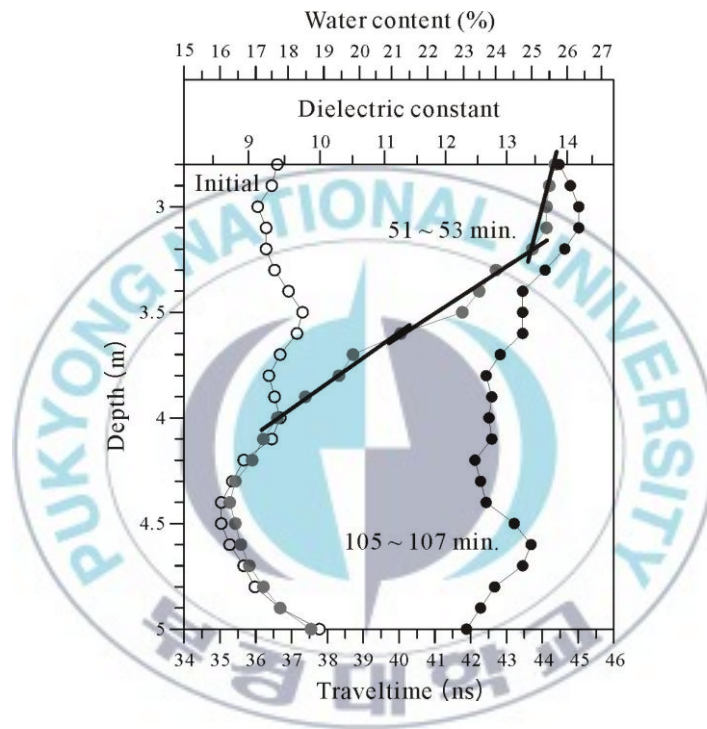
Fig. 4.2. First arrival times picked from time-lapse ZOP of radargrams obtained from the infiltration experiment. EM-wave velocities estimated by first arrival times are transformed into apparent dielectric constants and further converted to volumetric water contents. Three straight lines are shown for identifying critically refracted traveltimes at depths shallower than 4.0 m.

After calculating synthetic radargrams for the two dielectric constant profiles using the FDTD scheme, we pick the first arrival times (Fig. 4.4) in the same way as used for the field data in Fig. 2.2. The best fit to these data is obtained with the simple layered model which predicts the data to within a misfit (root-mean-squares of relative error) of 0.56 %, while the ZOP model produces 2.67 %. As expected, the relative error reduces significantly when accounting for critical refractions. There are many models which fit the data equally well due to non-uniqueness of the solution. As the number of layers increases, however, it becomes more difficult to identify each of the individual straight-line segments indicating critical refractions. Consequently, the
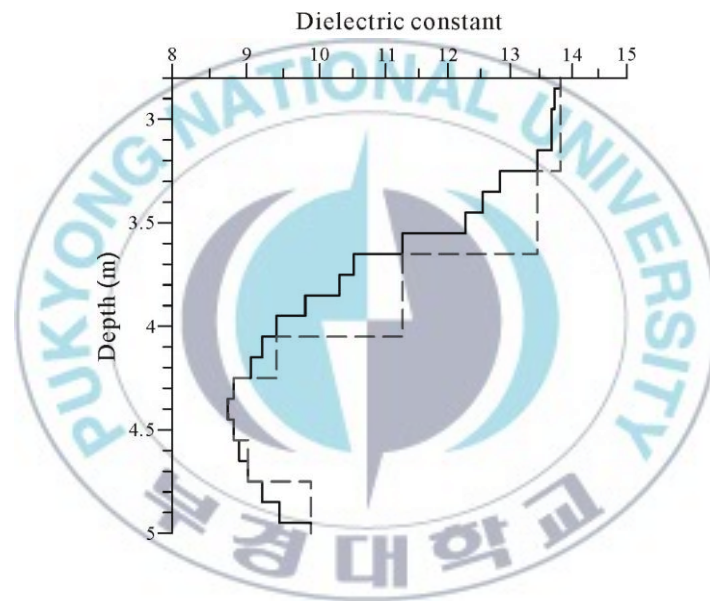
Fig. 4.3. Depth Profiles of dielectric constant derived from assuming all first arrival times are direct (solid) and considering critical refraction (dashed).
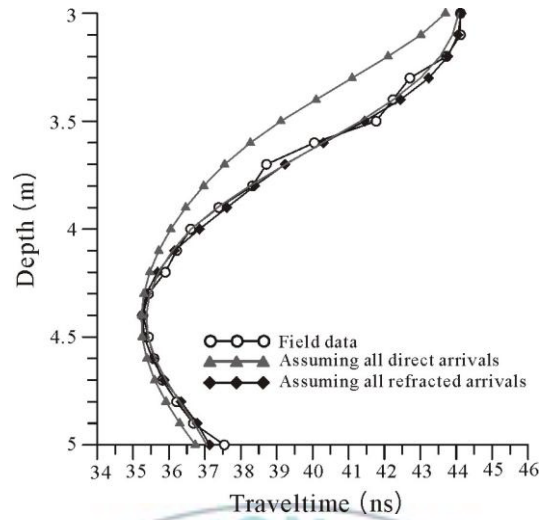
Fig. 4.4. Depth Profiles of first arrival times obtained from measured data (circles), and modeled for the dielectric constant profiles assuming all first arrivals are direct (triangles) and considering critical refractions (diamonds).

standard ZOP method in which all first arrivals are assumed to be direct waves results in a significant underestimation of the water content in the transition zone of 4.5 to 16 % as shown in Fig. 4.4.

Fig. 4.5 shows calculated radar traces at a point of 3.58 m horizontally from the center of a 1 m transmitter antenna for the dielectric constant profile obtained by considering critical refractions in Fig. 4.3. All traces are normalized by their maximum amplitudes. The synthetic radargrams correspond well to the field data, and thus successfully reproduces the major features of the field results. At depths shallower than 4.0 m, critically refracted waves arrive at the receivers prior to direct waves. However, it is difficult to identify these waves separately in the waveforms, because the offset between the transmitter and receiver is too short.
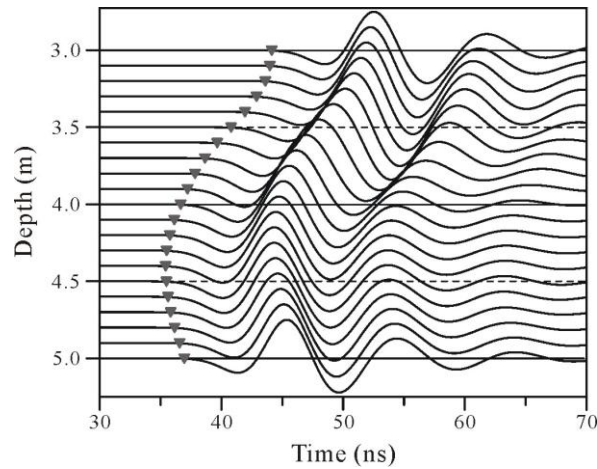
Fig. 4.5. Radargrams modeled for the dielectric constant profile considering critical refractions in Fig. 4.3. Electric fields are observed at a point of 3.58 m horizontally from the centre of a 1 m transmitter antenna located in an air-filled borehole with a diameter of 7 cm. Triangles show first arrival times.

4.4. Summary

Correct velocity analysis requires identification of first-arriving critically refracted waves from the traveltime profile to accurately determine the water content profile. After identifying the critically refracted first-arrivals with the slopes in the trvaltime profile, we obtained an accurate dielectric constant model which fit well with the field data. A FDTD solution of Maxwell's equations in 2D cylindrical coordinates was utilized to evaluate the dielectric permittivity accurately in the vadose zone and to simulate radargrams associated with the advance of the wetting front during the filtration process. The standard ZOP method results in 4.5 – 16 % underestimation of the water content in the transition zone above the wetting front.

Chapter 5. A shifted PAT method

5.1. Introduction

In this Chapter, we present an efficient algorithm to obtain an accurate dielectric constant model from ZOP data. The algorithm uses the maximum first-cycle amplitude to approximately determine the arrival time of direct waves. This method is tested and validated using a synthetic example. To interpret cross-borehole GPR data, we use a FDTD solution of Maxwell's equations in 2D cylindrical coordinates (Jang et al., 2007). The proposed method is then applied to real field data measured in the vadose zone during the infiltration experiment conducted in the Nagaoka site (Kuroda et al., 2007; 2009). Finally, the obtained water content model is compared with that derived using the standard ZOP analysis and conclusions are drawn.

5.2. Standard ZOP analysis

We first examine the standard ZOP analysis with a 5-layer model shown in Fig. 5.1a. This model is designed to have a significant contrast in dielectric constant so that critically refracted first arrivals are expected. The infiltration process may not be 1D because the vadose zone is heterogeneous. However, we approximate the infiltration process with ZOPs as 1D, because the standard ZOP method relies on determining the velocity of an EM wave that follows a horizontal raypath between transmitting and receiving antennas.

To interpret cross-borehole GPR data, we calculate EM fields radiated from a transmitter antenna using a FDTD modeling scheme developed in (Jang et al., 2007). The FDTD approach is conceptually simple, accurate for arbitrary complex models, and capable of accommodating realistic antenna designs. This method also allows for the explanation of reflected, refracted and diffracted waves. A grid consists of 370 × 600 cells, each of which is 1 cm by 1 cm and has a constant conductivity of 1 mS/m. A

1 m-long dipole antenna is used for the transmitting antenna. A source applied to the transmitter is a Gaussian voltage pulse with a pulse width of 2 ns. The horizontal distance between the transmitter and receiver is 3.58 m.
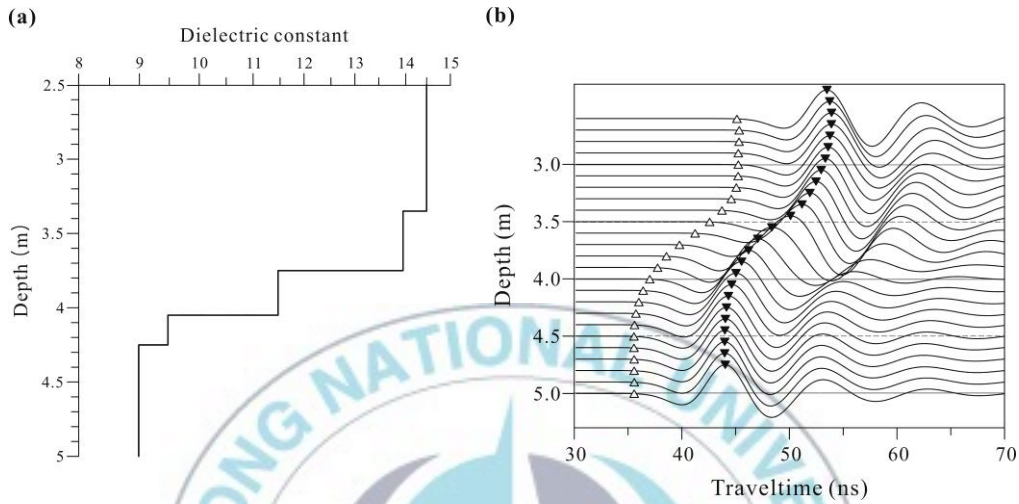
Fig. 5.1. Synthetic radargrams (b) generated for a 5-layered model (a) using the FDTD modeling scheme developed by Jang et al (2006). First arrivals (Δ) and maximum first-cycle amplitude (▼) are shown.

Fig. 5.1b shows synthetic radargrams for the dielectric constant model in Fig. 5.1a using the FDTD method. Each radar trace is normalized by its maximum amplitude. In the standard ZOP analysis, first arrivals are assumed to be direct waves and a dielectric constant model is derived via equation (1) as shown in Fig. 5.2a (grey solid). This illustration clearly shows that the standard ZOP method results in a significant underestimation of dielectric constant. After calculating synthetic radargrams for the dielectric constant model derived from the standard ZOP analysis, we can pick first arrivals as shown in Fig. 5.2b. The rms error of differences between first-arrival traveltimes for the given (dashed) and estimated (gray solid) models in Fig. 5.2a is 1.31 ns.
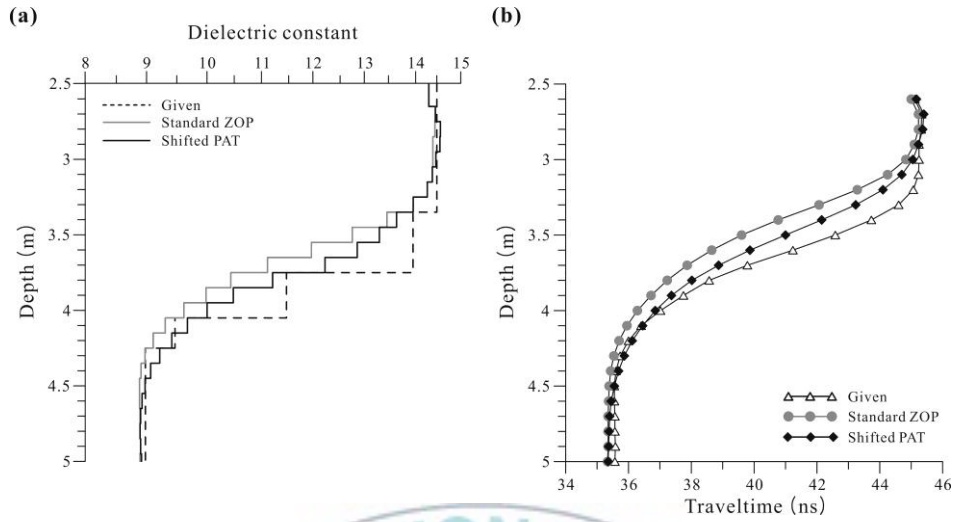
Fig. 5.2. First-arrival traveltimes (b) picked from synthetic radargrams calculated for dielectric constant models (a) derived from the traveltimes of first arrivals and shifted peak arrivals shown in Fig. 5.3. The given 5-layered model and the first arrivals are shown for comparison.
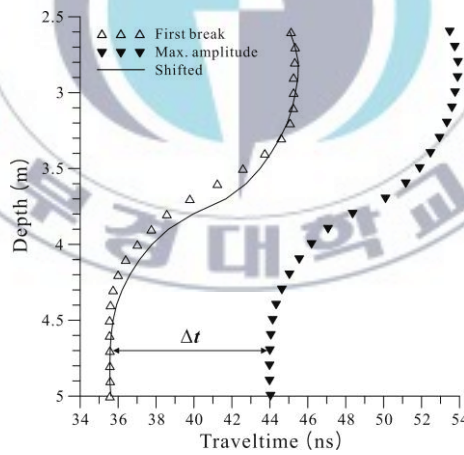
Fig. 5.3. A method showing a traveltime shift of maximum amplitudes, which is determined from the time difference between traveltimes of first arrival (Δ) and peak arrival (▼) at the least traveltime of the maximum first-cycle amplitude. The shifted traveltime profile is used to derive a dielectric constant model shown in Fig. 5.4a.

5.3. Shifted PAT method

An example of ZOP radargram gather is shown in Fig. 5.4, which is obtained in an intermediate state of about 47 minutes after the beginning of infiltration. The injected water can give rise to a wetting front between saturated and unsaturated zones. In other words, a sharp velocity contrast can be built in the vadose zone. In the intermediate state, first-arrival traveltimes are decreased significantly with depth in a zone shallower than 3.7 m. This is mainly attributed to decreased wetting with depth, and critically refracted waves may arrive prior to direct waves in the shallow zone. When GPR antennas are located within a high water content layer that is adjacent to a lower water content layer, critically refracted waves may arrive before direct waves. If the critically refracted waves are mistakenly interpreted to be direct waves, the water content will be underestimated.
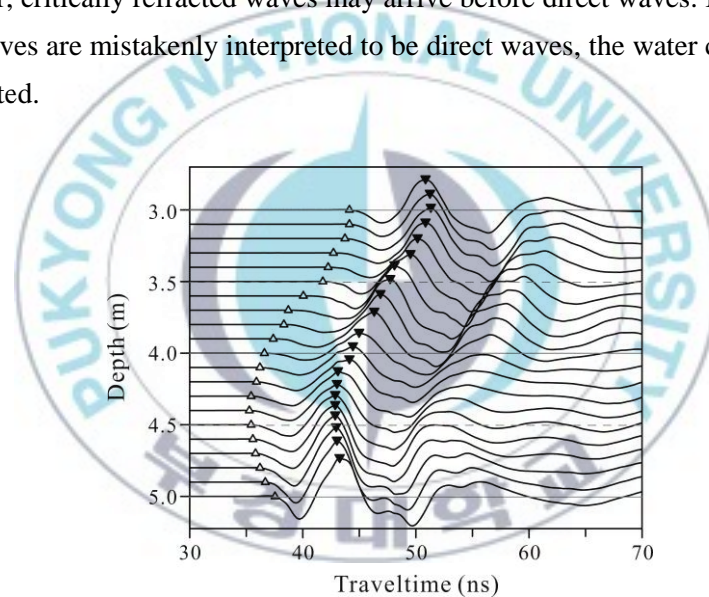
Fig. 5.4. Radargrams observed at 47 min after the beginning of the infiltration test. Triangles show the picked first arrival traveltimes. First arrivals (Δ) and peak arrivals ($\blacktriangledown$) are shown.

Use an exact dielectric constant model can be obtained from equation (1) only when first arrivals are direct waves. The underestimation in dielectric constant

estimates in the standard ZOP analysis is mainly due to the existence of critically refracted waves (Rucker and Ferre, 2004; Kuroda et al., 2009). To produce a more accurate dielectric constant model there may be three options: 1) identification of critically refracted waves, 2) ray-based velocity inversion of first-arrival traveltimes, and 3) estimation of direct-wave arrival times. Kuroda et al. (2009) used the first approach using a slope analysis of the traveltime versus depth profile to solve the problem of underestimation in dielectric constant estimates. However, this approach subjectively determines the number of layers. The second approach may be most accurate to build the dielectric constant model from the first-arrival traveltimes. However, it is not free from a non-uniqueness problem and requires iterative calculations to obtain a best-fit model. In this chapter, we concentrate on the third approach, which is an efficient procedure without iterative calculations as in the standard ZOP analysis.

Direct waves travel the shortest distance with a horizontal straight path in ZOP mode. In this regard, they have larger amplitudes than other waves, and may play a major role of forming the maximum first-cycle amplitude (peak) even in an area of critical refractions. In other words, a time difference between the peak and direct-wave arrivals is almost constant from trace to trace (Takahashi and Sato, 2006), although that between the peak and first arrivals is the result of many factors such as dispersion. In this study, we assume the time shift between the peak and direct-wave arrivals is constant from trace to trace. As a result, if the time shift is known from a trace, we can estimate the direct-wave arrival times of the other traces using the time shift. This assumption seems practically acceptable because there may not be very large change of dielectric constant in infiltration process.

Fig. 5.6 shows our scheme to estimate a direct-wave arrival from the peak arrival in each radar trace. Using the trace with the fastest peak-arrival traveltime (PAT), which occurs at a depth of 4.7 m, we can determine a time shift between the first and peak arrivals, Δt. In this trace, the direct wave appears as a first arrival. All PATs are then shifted by Δt. The shifted PAT is selected as a direct-wave arrival time if it is slower than the first-arrival traveltime. Conversely, the first-arrival traveltime is

chosen if it is slower than the shifted PAT, because no wave arrives before the first-arrival traveltime. We call this empirical scheme a shifted PAT method. Once the direct-wave arrival time is estimated, the dielectric constant and water content can be derived via equations (2.1) and (2.2), respectively.

Fig. 5.5a compares dielectric constant models derived from the standard ZOP analysis and the shifted PAT method. This illustration clearly shows that the shifted PAT method is effective to relieve the underestimation in dielectric constant estimates in the standard ZOP analysis especially at depths between 3.3 m and 4.0 m, where a significant variation of dielectric constant exists. Fig. 5.5b compares synthetic first-arrival traveltimes calculated for the dielectric constant models in Fig. 5.7a. Again, the shifted PAT method yields better fits on first-arrival traveltimes than the standard ZOP method. The rms error of differences between first-arrival traveltimes for the given (dashed) and estimated (black solid) dielectric constant models in Fig. 5.4b is 0.68 ns, about half of that (1.31 ns) obtained from the standard ZOP analysis.

Next, we apply the shifted PAT method to real field data measured in the Nagaoka site, which were shown in Fig. 5.2. After picking traveltimes of both first and peak arrivals, we determine a time shift Δt at a depth of 4.6 m (Fig. 5.5), where the fastest maximum first-cycle amplitude occurs. Direct arrival times are then estimated by using the shifted PAT method. Fig. 5.6a compares dielectric constant models derived from the standard ZOP analysis and shifted PAT method. At depths between 3.2 m and 4.0 m, the dielectric constant is significantly smaller in the conventional ZOP method than in the newly proposed method.

We further compare synthetic first-arrival traveltimes as shown in Fig. 5.6b, which are calculated for the two dielectric constant models in Fig. 5.6a, with observed ones in Fig. 5.4. The rms errors of the evaluated first arrivals are 0.47 ns and 1.17 ns for both models in Fig. 5.6a. Thus, the shifted PAT method is useful for alleviating the underestimation in dielectric constant estimates in the standard ZOP analysis. A more accurate dielectric constant model can be obtained from a slope analysis of the traveltime versus depth profile to adequately account for critical refractions (Kuroda et al., 2009). However, this approach subjectively determines the number of layers in
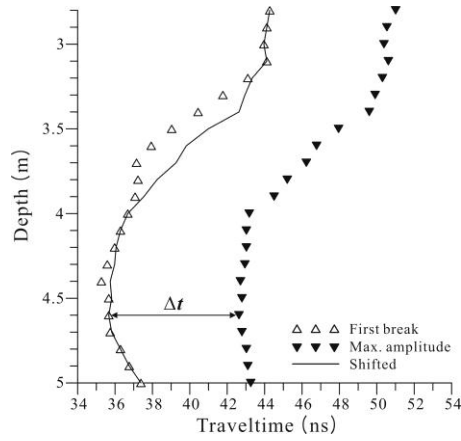
Fig. 5.5. A traveltime shift of peak arrivals determined at the least traveltime of the maximum first-cycle amplitude. The shifted traveltime profile is used to derive a dielectric constant model shown in Fig. 5.6a.
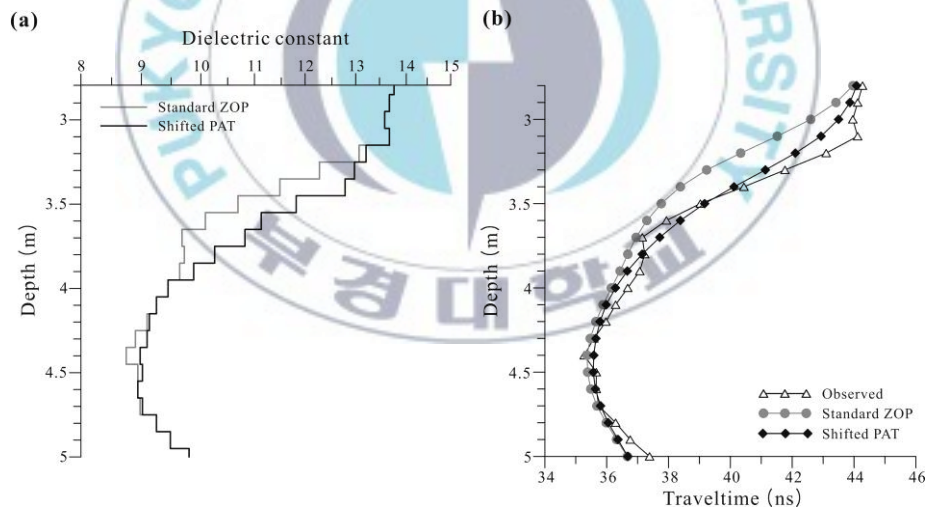
Fig.5.6. Dielectric constant models (a) derived from traveltimes of first arrivals and shifted peak arrivals of observed radargrams, and first-arrival traveltimes (b) picked from synthetic and observed radargrams.

layered models, and can produce many models which fit the data equally well due to non-uniqueness of the solution.

The dielectric constant can be transformed into the water content via equation (2.2). Fig. 5.7 compares time-lapse water content profiles estimated with the standard ZOP and shifted PAT methods. From the illustrations, we can find an increase of water content and the downward migration of induced water with time. Again, it is apparent that the standard ZOP analysis results in an underestimation of water content especially at shallow depths compared with the shifted PAT method. The zone at depths shallower than 3.7 m is considered to be fully saturated at $T = 61$ min, where T indicates the time after infiltration, because the water content profile estimated by the shifted PAT method is nearly identical to that at $T = 106$ min as shown in Fig. 5.8b. However, the standard ZOP analysis produces only an unsaturated profile at $T = 61$ min (Fig. 5.7a).

A wetting front, which is the boundary between the advancing water and relatively dry soil, can be defined as the depth at which water content begins to increase. In an early time profile at $T = 31$ min, for example, we can find the wetting front at a depth of 3.55 m above which water content is higher than that in the initial state. An interval between the initial and fully saturated states is considered to be a transition zone. Within the transition zone a sharp change of water content is found at depths of 3.45 m, 3.95 m, and 4.25 m in the profiles at $T = 42$, 47 and 52 min, respectively (Fig. 5.7b). These depths are 30 – 40 cm deeper than those derived from the standard ZOP analysis. In particular, such a steep increase of water content is obtained from the shifted PAT method at a depth of 2.95 m even in the early time profile at $T = 31$ min, while not clear in the standard ZOP analysis. In the zone above that in which there is a steep increase of water content, critically refracted waves are first to arrive. The effect of critically refracted waves is allowed in the shifted PAT method, whereas not in the ZOP analysis.
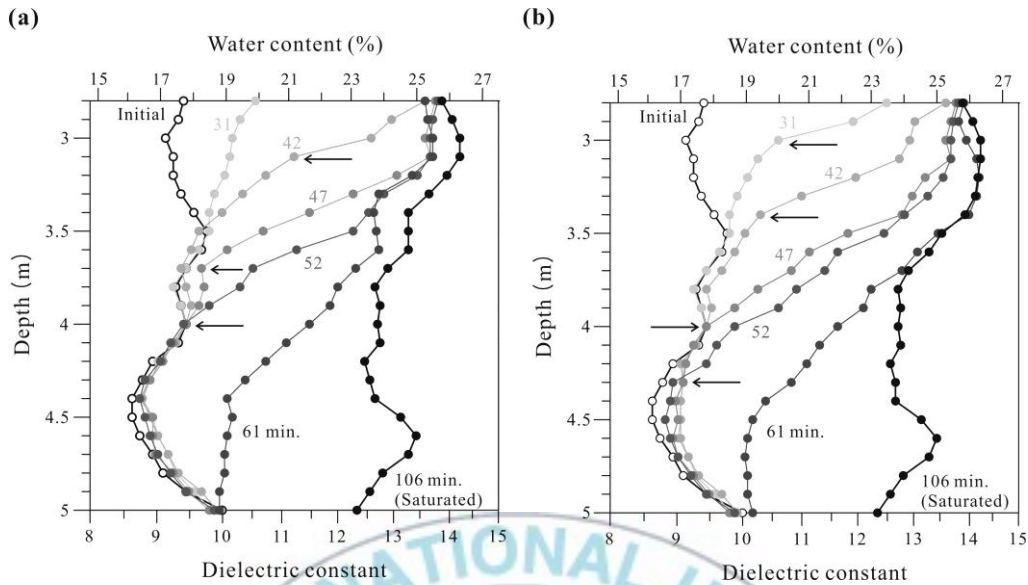
Fig. 5.7. Volumetric water content profiles estimated from the standard ZOP analysis (a) and the shifted PAT method (b) during the infiltration process. Arrows indicate a sharp increase of water content.

5.4. Summary

We introduced an efficient scheme to derive a dielectric constant model more accurately than the standard ZOP analysis from ZOP data. This scheme, called a shifted PAT method, uses the maximum first-cycle amplitude to approximately identify the arrival time of direct wave, and is effective in building an accurate dielectric constant model without iterative calculations as in the standard ZOP analysis. Superiority of the shifted PAT method over the standard ZOP analysis has been tested on synthetic and real field data. The difference between measured and modeled first-arrival traveltimes is largely reduced in the shifted PAT method compared with the conventional ZOP method.

The variation of volumetric soil water content in the Nagaoka site can be estimated from the time-lapse ZOP data measured in the artificial infiltration

experiment. This newly developed method enables us to draw a reliable characterization of the vadose zone, in which induced water moves rapidly. We can find a steep increase of water content in the transition zone even in the early time profile at T = 31 min at a depth of 2.95 m, while it is not clear in the standard ZOP analysis. One hour after the beginning of the infiltration, an upper half of the whole range in the test zone is considered to be fully saturated, whereas the standard ZOP analysis produces only an unsaturated profile. In the transition zone, critically refracted waves are likely to arrive prior to direct waves.

Chapter 6. SVD inversion of zero-offset profiling data

6.1. Introduction

In ZOP mode, an EM wave velocity is usually calculated for a known antenna separation, assuming that the first-arriving EM energy travels along a straight path from the transmitter to the receiver. This standard ZOP analysis, however, can give rise to erroneous velocity estimates if refracted waves are first to arrive (Huisman et al, 2003; Rucker and Ferre, 2004), and results in an underestimation of water content estimates in the transition zone above a wetting front (Kuroda et al., 2008; Jang et al., 2011a). To solve the problem of underestimation, Kuroda et al. (2008) used a slop analysis of the traveltime versus depth profile, while Jang et al. (2011a) utilized the maximum first-cycle amplitude to derive the direct-wave arrival time.

We present an inversion approach to derive an accurate dielectric constant model from ZOP data. This approach is based on a least-squares inversion method using singular value decomposition (SVD), tested on a synthetic example, and applied to the field data measured in the vadose zone during the infiltration experiment in Nagaoka, Japan (Kuroda et al., 2007; 2008). We use a FDTD solution of Maxwell's equations in 2D cylindrical coordinates to simulate GPR wavefields (Jang et al., 2007). The variation in soil water content in the vadose zone is estimated from the reconstructed dielectric constant models.

6.2. SVD inversion

A least-squares inversion scheme is used to derive a dielectric constant distribution in a medium between two boreholes. A linearized inverse problem can be expressed as

$$\mathbf{J}\Delta\mathbf{m} = \Delta\mathbf{d}, \tag{6.1}$$

where $\mathbf{J}$ is the Jacobian matrix or derivatives of model responses with respect to model parameters, $\Delta\mathbf{m}$ is a correction vector to the model parameters, and $\Delta\mathbf{d}$ is a misfit vector between observed and modeled data. The Jacobian matrix can be calculated from forward modeling with a FDTD solution of Maxwell's equations in 2D cylindrical coordinates (Jang et al., 2007; 2011a)

The inverse problem is equivalent to minimization of the difference between observed and modeled data. Hence, the objective of inversion is to find a model of dielectric constant distribution that adequately reproduces the observed data. From equation (6.1), the model correction vector $\Delta\mathbf{m}$ can be obtained as

$$\Delta\mathbf{m} = (\mathbf{J}^{\mathrm{T}}\mathbf{J})^{-1}\mathbf{J}^{\mathrm{T}}\Delta\mathbf{d}, \tag{6.2}$$

where superscript T indicates matrix transpose. We can solve this equation by using the SVD of $\mathbf{J}$ as (Golub and van Loan, 1996; Menke, 1989)

$$\mathbf{J} = \mathbf{U}\mathbf{\Lambda}\mathbf{V}^{\mathrm{T}}, \tag{6.3}$$

where $\mathbf{U}$ is a matrix of singular vector in data space, $\mathbf{V}$ is a matrix of singular vectors (or basis functions) in model space and $\mathbf{\Lambda}$ is an ordered diagonal matrix of decreasing singular values.

The reconstructed SVD solution $\Delta\mathbf{m}$ is given by

$$\Delta\mathbf{m} = \mathbf{V}\mathbf{V}^{\mathrm{T}}\Delta\mathbf{m} = \mathbf{V}\mathbf{\Lambda}^{-1}\mathbf{U}^{\mathrm{T}}\Delta\mathbf{d}, \tag{6.4}$$

where $\mathbf{V}\mathbf{V}^{\mathrm{T}}$ is the resolution matrix. This equation can be written alternatively as (Golub and van Loan, 1996)

$$\Delta \mathbf{m} = \sum_{j=1}^{k} \left(\frac{U_j^{\mathrm{T}} \Delta \mathbf{d}}{\Lambda_j} \right) V_j \, , \tag{6.5}$$

where k denotes the number of singular values. To choose an optimal number of singular values we use the L-curve method (Hansen, 1992). The truncated SVD method avoids subjectivity from any empirically defined smoothness constraints, and gives a means of evaluating the model resolution and covariance from the resolution matrix (Friedel, 2003). Although the method is computationally expensive, the computation cost is not main concern in 1D inverse problems such as considered in this chapter.

Once $\Delta \mathbf{m}$ is obtained, the model is updated as

$$\mathbf{m}^{(l)} = \mathbf{m}^{(l\text{-}1)} + \Delta \mathbf{m}, \tag{6.6}$$

where l indicates the iteration number in the inversion process. To quantify the level of data fits, we defines a data misfit E as

$$E = \sqrt{\frac{\Delta \mathbf{d}^{\mathrm{T}} \Delta \mathbf{d}}{n}} \, . \tag{6.7}$$

where n is the number of data.

6.3. Validation on synthetic example

We first examine the standard ZOP analysis with a 5-layer model shown in Fig. 6.1a. This model is designed to have a significant contrast in dielectric constant so that critically refracted first arrivals are expected. The infiltration process may not be 1D because the vadose zone is heterogeneous. However, we approximate the infiltration process with ZOPs as 1D, because the standard ZOP method relies on determining the velocity of an EM wave that follows a horizontal raypath between transmitting and

receiving antennas.

Unlike classical 2D inversions which divide the medium into many cells, we divide the medium into layers. This type of 1D parameterization reduces the number of unknowns and the problem becomes better-behaved (Lazaratos and Marion, 1997; Washbourne, 2002). The problem is further stabilized by truncating small singular values in SVD inversion. Sedimentary media are formed from materials that have been displaced from where they originated by either wind or water. They are commonly found in river flood plains as well as in arid wind-blown areas. It can be so generally decomposed in a sequence of layers.

To generate synthetic radargrams, we calculate EM fields radiated from a transmitter antenna using a FDTD modeling scheme developed by Jang et al. (2007). The FDTD approach is conceptually simple, accurate for arbitrary complex models, and capable of accommodating realistic antenna designs. This method also allows explaining reflected, refracted and diffracted waves as well. A grid consists of 370×600 cells, each of which is 1 cm by 1 cm. A 1 m long dipole antenna used for the transmitting antenna. A source applied to the transmitter is a Gaussian voltage pulse with a pulse width of 2 ns (Kuroda et al., 2008).

Fig. 6.1b shows the calculated radargrams for the dielectric constant model shown in Fig. 6.1a. Each radar trace is normalized by its maximum amplitude. In the standard ZOP method, first arrivals are assumed to be direct waves and a dielectric constant model is derived via equation (1) as shown in Fig. 6.2a. After calculating synthetic radargrams for the dielectric constant model using the FDTD method, we can pick first arrivals as in Fig. 6.2b. This illustration clearly shows that the standard ZOP method results in significantly lower estimates of dielectric constant. The rms error of differences between first-arrival times for the given and estimated models in Fig. 6.4a is 0.85 ns.
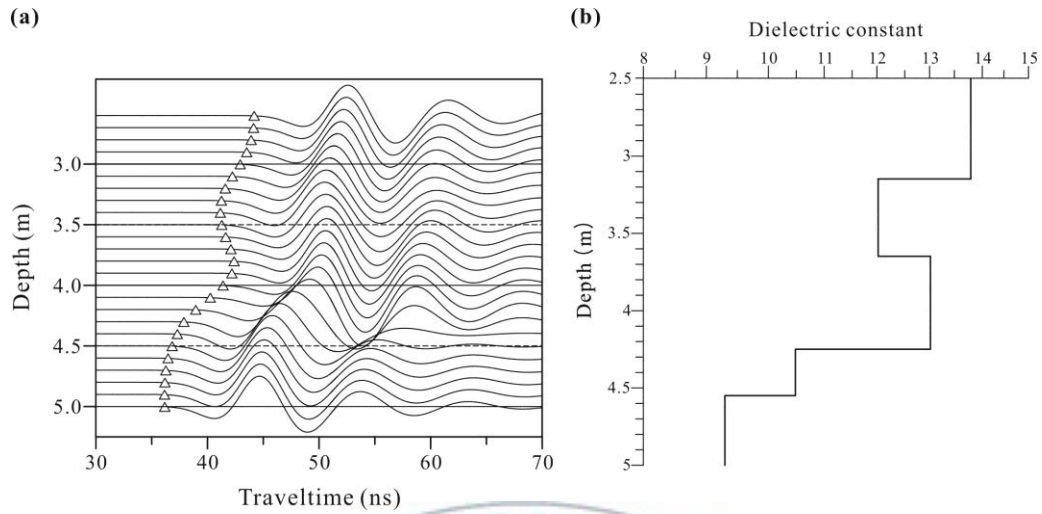
Fig. 6.1. Synthetic radargrams (a) generated for a 5-layered model (b) using the FDTD modeling scheme developed by Jang et al. (2007). Triangles show picked first-arrival traveltimes.

The dielectric constant model derived from the standard ZOP method can be improved by use of the SVD inversion algorithm described in the previous section. In the SVD inversion, the rms error was reduced to 0.13 ns and changed insignificantly after four iterations (Fig. 6.2b). This final error level is much lower than that (0.85 ns) in the standard ZOP method. Fig. 6.2a compares dielectric constant models derived from the conventional ZOP analysis and the SVD inversion method. From the reconstructed models we can find that the SVD inversion is effective to reduce the underestimation in dielectric constant especially at depths between 3.6 m and 4.5 m.
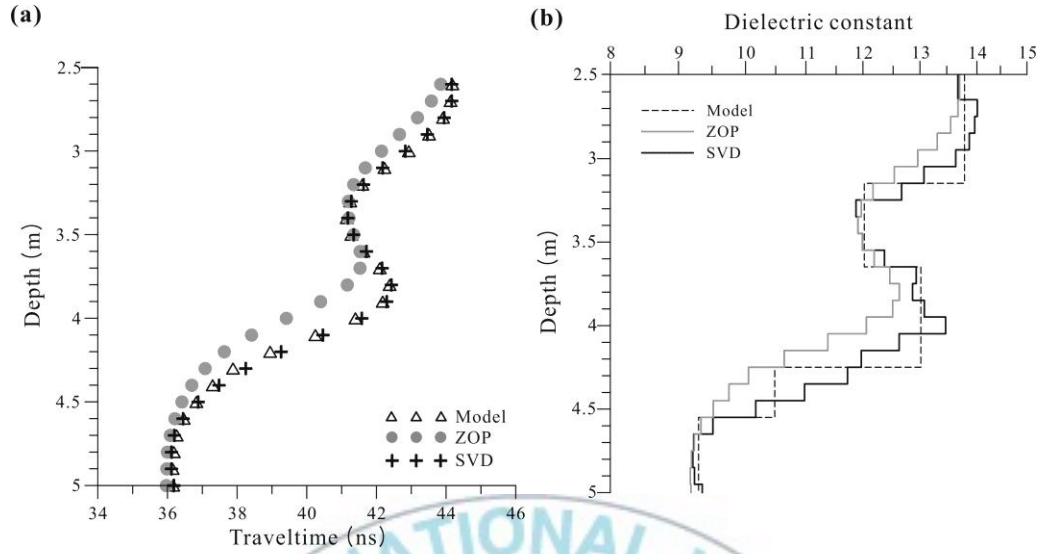
Fig. 6.2. First-arrival traveltimes (a) picked from synthetic radargrams calculated for dielectric constant models (b) derived from the standard ZOP analysis and SVD inversion. The given 5-layered model and the first-arrival traveltimes in Fig. 6.1 are also shown for comparison.

6.4. Characterization of the Nagaoka site

Next, we applied the SVD inversion method to the field data (T = 52 min in Fig. 2.2) to estimate a variation of soil water content in the vadose zone. The initial model in Fig. 6.3a (dashed line) is derived from the standard ZOP method. The inversion of first-arrival traveltimes is terminated after three iterations with stable convergence as shown in Fig. 6.4 to produce a reasonable model (solid line in Fig. 6.3a), whose dielectric constants are recovered to be higher than those from the standard ZOP analysis. After calculating synthetic radargrams for the reconstructed dielectric constant model, we compared their first-arrival traveltimes with observed ones. The synthetic traveltime profile (crosses in Fig. 6.3b) is well fitted with the field data (triangles); the final rms data error reduced from 1.1 ns to 0.2 ns (Fig. 6.4). From the dielectric constant models,

we can find again that the standard ZOP method results in significantly lower estimates of soil water content.
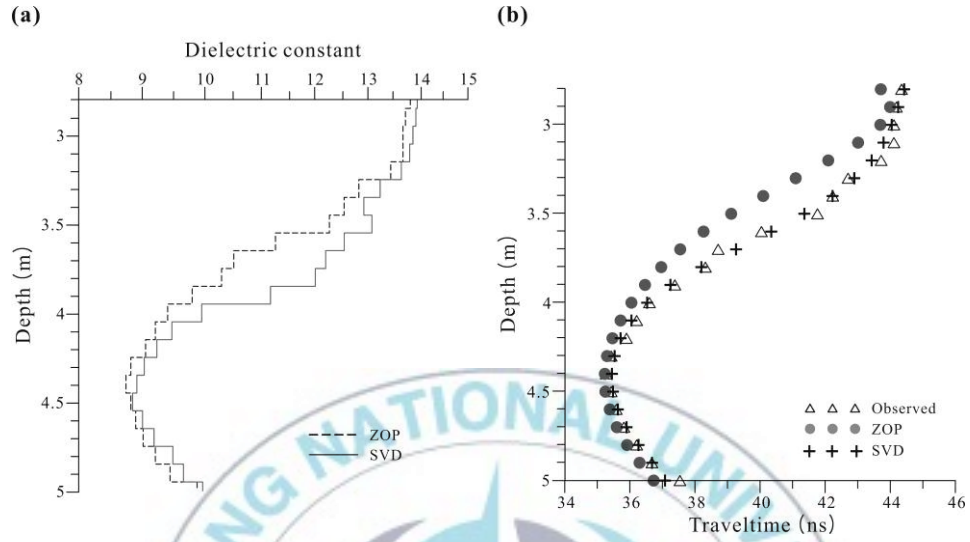
Fig. 6.3. (a) Dielectric constant models at $T = 52$ min derived from the standard ZOP method (dashed) and SVD inversion (solid). (b) Depth profiles of first-arrival traveltimes observed (triangles), and obtained from the standard ZOP method (circles) and SVD inversion (crosses).
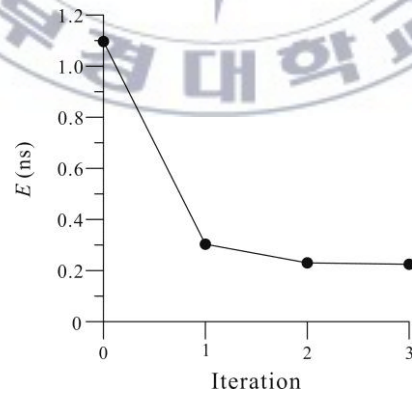
Fig. 6.4. Data misfits during SVD inversion of the traveltime data at $T = 52$ min.
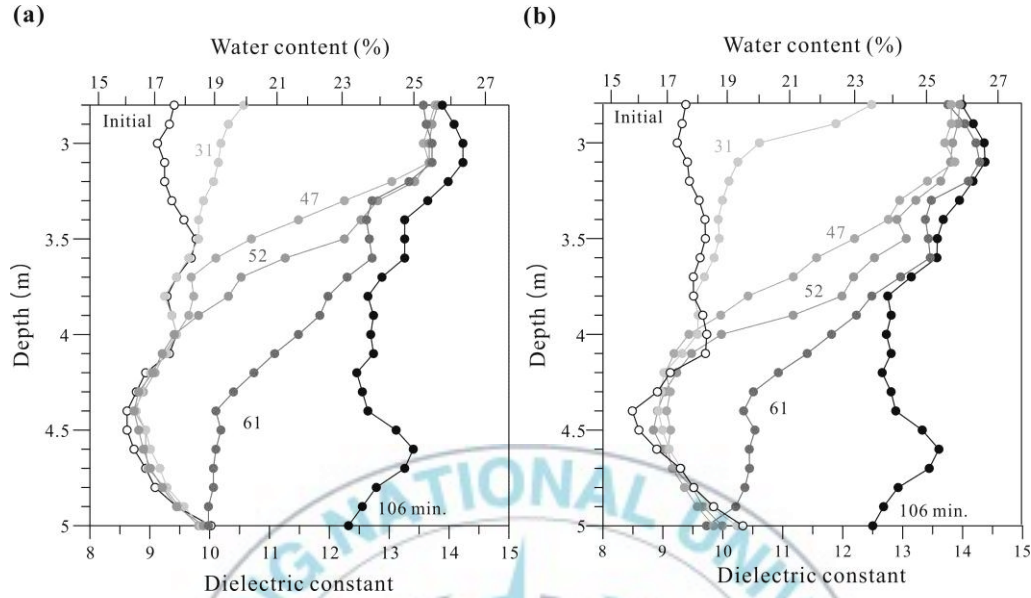
Fig. 6.5. Volumetric water content profiles estimated from the standard ZOP analysis (a) and SVD inversion (b) during the infiltration process.

Fig. 6.5 compares time-lapse water content profiles estimated with the standard ZOP and SVD inversion methods. From the illustrations, we can see an increase in water content and the downward migration of induced water with time. Again, it is apparent that the standard ZOP analysis results in lower estimates of water content, particularly at shallow depths, compared with the SVD inversion method. The zone shallower than 3.5 m is considered to be maximally saturated at $T = 61$ min because the water content profile is nearly identical to that at $T = 106$ min as in Fig. 6.5b.However, the standard ZOP analysis produces only an unsaturated profile at $T = 61$ min (Fig. 6.5a).

In an early time profile of $T = 31$ min, we can find a wetting front at a depth of 3.5 m above which water content is higher than that in the initial state. An interval between the initial and maximally saturated states is considered to be a transition zone. Within the transition zone, a sharp change of water content is found at a depth of 4 m

at T = 47 min (Fig. 6.5b). The depth is about 60 cm deeper than that derived from the standard ZOP analysis. In particular, such a steep increase in water content is obtained at 3 m even in the early time profile of T = 31 min, whereas it is not clear in the standard ZOP analysis. In the zone above that in which there is a steep increase in water content, critically refracted waves are considered to be first to arrive.
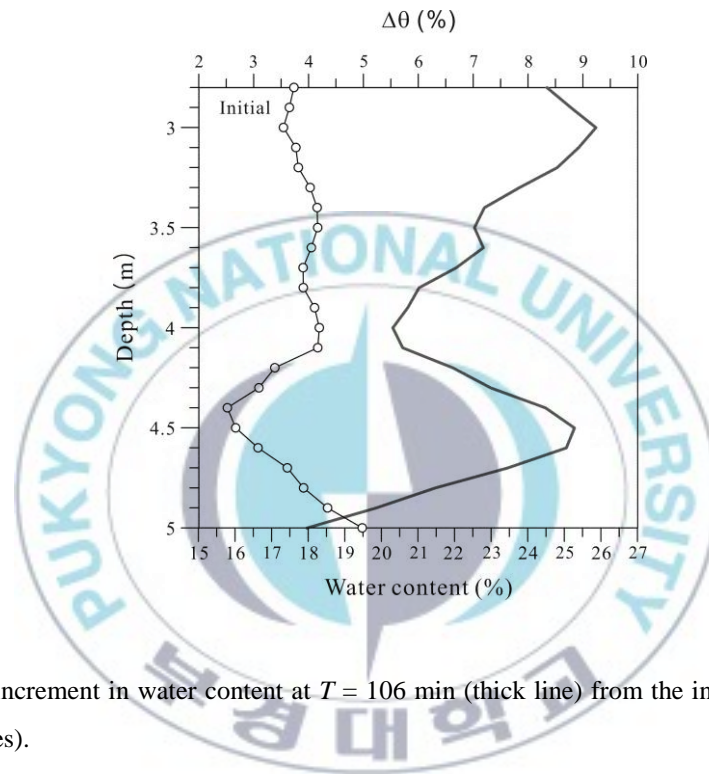
Fig. 6.6. An increment in water content at T = 106 min (thick line) from the initial state (open circles).

The infiltration process in the Nagaoka site is clearly observed as a variation of water content profiles with time (Fig. 6.5b). In the initial (unsaturated) state, soil water content ranges from 16 – 19% except below 4.8 m; the maximum and minimum water contents are found at depths of 3.4 m and 4.5 m, respectively. In the intermediate state (T = 52 min), water content is increased from the initial state at depths shallower than 4.0 m with almost no change in the deep zone. In particular, at depths between 3.5 and 4.0 m water content varies significantly with depth. In the later state (T = 106 min),

water content increases to 23 – 27%. In general, it decreases slightly with depth, whereas increases locally in zones around 3.0 m and 4.6 m. Since water content begins to decrease again from the shallow zone after $T = 106$ min (not shown), this state can be regarded as a maximally saturated state.

The maximally saturated state is helpful to know how much water can be stored in the vadose zone. In other words, we can estimate effective porosity of the medium from the maximally saturated state. In contrast, the initial state partly reflects the grain size of the medium; lower water content indicates a layer with larger grains, and vice versa. Furthermore, the shape of water content profiles shows an opposite characteristics between the initial and maximally saturated states. For example, two zones around 3.0 m and 4.6 m have locally maximum values in water content at $T = 106$ min, whereas locally minimum values in the initial state. A change in water content between the two states is shown in Fig. 6.6. From the illustration, we can see clear peaks at depths of 3.0 m and 4.5 m. This may indicate that these zones consist of relatively large grains with large pore space. On the contrary, a depth of 4.0 m reveals a least increase of water content in the test zone above 4.8 m, suggesting a relatively impermeable layer. This fact may be confirmed also in Fig. 6.5b; water content rapidly increases in the shallow zone but does not change below 4.0 m until $T = 61$ min.

6.5. Summary

An artificial groundwater infiltration test was performed in Nagaoka, Japan, and time-lapse borehole GPR data were acquired in ZOP mode to monitor the infiltration process in the vadose zone. Although ZOPs provide only 1D integrated velocity profiles, the infiltration process is clearly observed as a variation of EM-wave traveltimes, which can be transformed into dielectric constant and further converted to water content. In this chapter, we utilized a least-squares inversion method using SVD to estimate the structure of dielectric constant in the Nagaoka site form the ZOP data. The SVD inversion method was quite effective to reduce the underestimation in dielectric constant estimates derived from the conventional ZOP analysis for which all

first arrivals are assumed to be direct waves.

   With the reconstructed dielectric constant models, we successfully estimated a variation of soil water content, which is associated with an advancing wetting front during infiltration in the Nagaoka site. The soil water content varied significantly from 16 – 19% in the initial state to 23 – 27% after the maximum saturation. The shape of water content profiles shows an opposite characteristics between the unsaturated and maximally saturated states. The saturation information is useful to assess hydrogeologic properties of the soil such as pore space and grain size.

Chapter 7. Conclusions

An artificial groundwater infiltration test was performed in Nagaoka, Japan, and time-lapse borehole GPR data were acquired in ZOP mode to monitor the infiltration process in the vadose zone. The infiltration process is clearly observed as a variation of EM-wave traveltimes, which can be transformed into a dielectric constant and further converted to water content using Topp's equation. The time-lapse ZOP data measured in the artificial infiltration experiment enables us to draw a reliable characterization of the vadose zone in which induced water moves rapidly.

A FDTD solution of Maxwell's equations in 2D cylindrical coordinates was utilized to evaluate the dielectric permittivity accurately in the vadose zone and to simulate radargrams associated with the advance of thewetting front during the filtration process. We presented a FD solution of Maxwell's equations in cylindrical coordinates which is suitable for modelling crosshole GPR data. This algorithm was used to model the EM wavefield radiated from a vertical electric antenna located in a borehole filled with air or water. Major simplifications made in this study were that only the radiation pattern of the transmitter was accounted for explicitly and that the received signal was represented by the electric field at the observation point. The radiation pattern of an antenna located in a water-filled borehole is severely distorted by a waveguide effect that depends on the length of the transmitter antenna, the medium filling the borehole, and the diameter of the borehole. Given that most shallow boreholes are at least partially water-filled, this has potentially serious implications for the interpretation of crosshole GPR data. Further complications of the radiation pattern, regardless of the medium filling the borehole, must be expected to arise from vertical stratification and lateral heterogeneity of electric parameters in the shallow subsurface.

GPR responses in the vadose zone are largely controlled by variations in water saturation. Although ZOP provides only a 1D integrated profile of volumetric water content estimates, it is a simple tool for detecting the variation of the water content, which is associated with the advancing wetting front during the filtration process. An

increase in traveltimes can be attributed to an increase in water saturation, and the standard ZOP method allows us to estimate that the wetting front moves downward with an average velocity of about 2.7 m/h in the test zone. However, the standard ZOP analysis for which all first arrivals are assumed to be direct waves results in a significant underestimation of the dielectric constant due to the existence of critically refracted waves. To accurately determine the water content profile, correct velocity analysis requires identification of first-arriving critically refracted waves from the traveltime profile. After identifying the critically refracted first-arrivals with the slopes in the traveltime profile, we obtained an accurate dielectric constant model which fit well with the field data. The standard ZOP method results in 4.5–16% underestimation of thewater content in the transition zone above the wetting front.

Then we introduced an efficient scheme to derive a dielectric constant model more accurately than the standard ZOP analysis from ZOP data. This scheme, which is called the shifted PAT method, uses the maximum first-cycle amplitude to approximately identify the arrival time of the direct wave and is effective in building an accurate dielectric constant model without iterative calculations as in the standard ZOP analysis. Superiority of the shifted PAT method over the standard ZOP analysis has been tested on synthetic and real field data. The difference between measured and modeled first-arrival traveltimes is largely reduced in the shifted PAT method compared with the conventional ZOP method. We can find a steep increase in the water content in the transition zone even in the early time profile at $T = 31$ min at a depth of 2.95 m, whereas it is not clear in the standard ZOP analysis. One hour after the beginning of the infiltration, an upper half of the whole range in the test zone is considered to be fully saturated, whereas the standard ZOP analysis produces only an unsaturated profile. In the transition zone, critically refracted waves are likely to arrive prior to direct waves.

Finally, we utilized a least-squares inversion method using SVD to estimate the structure of the dielectric constant in the Nagaoka site from the ZOP data. The SVD inversion method was quite effective in reducing the underestimation in dielectric constant estimates derived from the conventional ZOP analysis for which all first

arrivals are assumed to be direct waves. With the reconstructed dielectric constant models, we successfully estimated a variation of soil water content, which is associated with an advancing wetting front during infiltration in the Nagaoka site. The soil water content varied significantly from 16%−19% in the initial state to 23%−27% after the maximum saturation. The shape of the water content profiles shows opposite characteristics between the unsaturated and maximally saturated states. The saturation information is useful to assess hydrogeologic properties of the soil such as pore space and grain size.

References

Alumbaugh, D., Chang, P. Y., Paprocki, L., Brainard, J. R., Glass, R. J., and Rautman, C. A., 2002: Estimating moisture contents in the vadose zone using cross-borehole ground penetrating radar: A study of accuracy and repeatability: *Water Resources Research*, **38**, 1309−1320.

Berenger, J. P., 1994, A perfectly matched layer for the absorption of electromagnetic waves: *Journal of Computational Physics*, **114**, 185–200.

Bergmann, T., Blanch, J. O., Robertsson, A., and Holliger, K., 1999, A simplified Lax-Wendroff correction for staggered-grid FDTD modeling of electromagnetic wave propagation in frequency-dependent media: *Geophysics*, **64**, 1369–1377.

Binley, A., Winship, P., Middleton, R., Pokar, M., and West, J., 2001, High-resolution characterization of vadose zone dynamics using cross-borehole radar: *Water Resources Research*, **37**, 2639−2652.

Binley, A., Cassiani, G., Middleton, R., and Winship, P., 2002, Vadose zone flow model parameterisation using cross-borehole radar and resistivity imaging: *Journal of Hydrol*ogy, **267**, 147-159.

Cassiani, G., Strobbia, C., Gallotti, L., 2004, Vertical radar profiles of deep vadose zone: *Vadose Zone Journal*, 3, 1093–1105.

Cassiani, G., A.M. Binley and T.P.A. Ferré., 2006, Unsaturated zone processes: *In* H. Vereecken et al. (ed.) *Applied hydrogeophysics*: Springer-Verlag, **71**. 75–116.

Chang, P.-Y., Alumbaugh, D., Brainard, J., Hall, L., 2006, Cross-borehole ground penetrating radar for monitoring and imaging solute transport within the vadose zone: *Water Resources Research*, **42**, W10413.

Davis, J. L., and Annan, A. P., 1989, Ground-penetrating radar for high-resolution mapping of soil and rock stratigraphy: *Geophysical Prospecting*, **37**, 531-551.

Day-Lewis, F. D., Lane, J. W., Harris, J. M., and Gorelick, S. M., 2003, Time-lapse imaging of saline tracer transport in fractured rock using difference radar attenuation tomography: *Water Resources Research*, **39**, 1290-13031.

Deiana, R., Cassiani, G., Kemna, A., Villa, A., Bruno, V., and Bagliani, A, 2007, An experiment of non-invasive characterization for the vadose zone via water injection and cross-hole time-lapse geophysical monitoring: *Near Surface Geophysics*, **5**, 183-194.

Deiana, R., Cassiani, G., Villa, A., Bagliani, A., and Bruno, V., 2008, Calibration of a vadose zone model using water injection monitored by GPR and electrical resistance tomography: *Vadose Zone Journal*, **7**, 183-194.

Ebihara, S., Sato, M., and Niitsuma, H., 1998, Analysis of a guided wave along a conducting structure in a borehole: *Geophysical Prospecting*, **46**, 489-505.

Ellefsen, K. J., and Wright, D. L., 2005, Radiation pattern of a borehole radar antenna: *Geophysics*, **70**, K1–K11.

Ernst, J. R., Holliger, K., Maurer, H., and Green, A. G., 2006, Realistic FDTD modelling of borehole georadar antenna radiation: methodology and application: *Near Surface Geophysics*, **4**, 19-30.

Friedel, S., 2003, Resolution, stability and efficiency of resistivity tomography estimated from a generalized inverse approach: *Geophysical Journal International*, **153**, 305-316.

Fullagar, P. K., Livelybrooks, D. W., Zhang, P., and Calvert, A. J., 2000, Radio tomography and borehole radar delineation of the McConnell nickel sulfide deposit, Sudbury, Ontario, Canada: *Geophysics*, **65**, 1920–1930.

Golub, G. H., and Van Loan, C. F., 1996, *Matrix Computations 3/e*: The John Hopkins University Press.

Hammon III,W.S., Zeng, X., Corbeanu, R.M., McMechan, G.A., 2002, Estimation of the spatial distribution of fluid permeability from surface and tomographic GPR data and core, with a 2-D example from the Ferron Sandstone, Utah: *Geophysics*, **67**, 1505–1515.

Hansen, P. C., 1992, Analysis of discrete ill-posed problems by means of the L-curve: *SIAM Review*, **34**, 561-580.

Holliger, K., and Bergmann, T., 2002, Numerical modeling of borehole georadar data: *Geophysics*, **67**, 1249–1257.

Huisman, J. A., Hubbard, J. D., Redman, J. D., and Annan, A. P., 2003, Measuring soil water content with ground penetrating radar: a review: *Vadose Zone Journal.*, **2**, 476-491.

Jang, H., Park, M. K., Kim, H. J., 2007, Numerical modelling of electromagnetic waveguide effects on crosshole radar measurements: *Exploration Geophysics*, **38**, 69-76.

Jang, H., Kuroda, S., and Kim, H. J., 2011a, Efficient electromagnetic imaging of an artificial infiltration process in the vadose zone using cross-borehole radar: *IEEE Geoscience Remote Sensing Letters*, **8**, 243-247.

Jang, H., Kuroda, S., and Kim, H. J., 2011b, SVD inversion of zero-offset profiling data obtained in the vadose zone using cross-borehole radar: *IEEE Trasactions on Geoscience and Remote Sensing*, **49**, 3849-3855.

King, R. W. P., and Smith, G. S., 1981, *Antennas in Matter*: *Fundamentals, Theory, and Applications*: MIT Press.

Kowalsky, M.B., Finsterle, S., Peterson, J., Hubbard, S., Rubin, Y., Majer, E., Ward, A., Gee, G., 2005, Estimation of field-scale soil hydraulic and dielectric parameters through joint inversion of GPR and hydrological data: *Water Resources Research*, **41**, W11425.

Kuroda, S., Satto, H., Okuyama, T., Takeuchi, J., Simunek, J., and Van Genuchten, M. TH., 2006, Quasi 3D image construction of infiltration processes in the vadose zone by combining inter borehole radar data and numerical simulation of water-flow in soils: *Proceedings of the 8th SEGJ International Symposium*, 128-131.

Kuroda, S., Asano, M., Nihira, S., Okuyama, T., Saito, H., Kim, H. J., and Takeuchi, M., 2007, Quantitative estimation of groundwater recharge process through a vadose zone using time-lapse cross-borehole radar profiling: *Butsuri-Tansa* (*Geophysical Exploration*), 60, 467-476. (in Japanese)

Kuroda, S., Jang, H., and Kim, H. J., 2009, Time-lapse borehole radar monitoring of an infiltration experiment in the vadose zone: *Journal of Applied Geophysics,* **67**, 361-366.

Lane, J. W., Day-Lewis, F. D., and Casey, C. C., 2006, Geophysical monitoring of a field-scale biostimulation pilot project: *Ground Water*, 44, 430-443.

Lazaratos, S., and Marion, B., 1997, Crosswell seismic imaging of reservoir changes causing by CO_2 injection: *The Leading Edge*, **16**, 1300–1308.

Menke, W., 1989, *Geophysical Data Analysis*: *Discrete Inverse Theory*: Academic Press.

Moran, M. L., and Greenfield, R. J., 1993, Radar signature of a 2.5-D tunnel: *Geophysics*, **58**, 1573–1587.

Moysey, S., and Knight, R. J., 2004, Modeling the field-scale relationship between dielectric constant and water content in heterogeneous systems: *Water Resources Research.*, **40**, 3510-3519.

Olhoeft, G. R., 1988, Interpretation of hole-to-hole radar measurements: *Proceedings of the 3rd Symposium on Tunnel Detection*, 616–629.

Olsson, O., Falk, L., Forslund, O., Lundmark, L., and Sandberg, E., 1992, Borehole radar applied to the characterization of hydraulically conductive fracture zones in crystalline rock: *Geophysical Prospecting*, **40**, 104–116.

Pratt, R. G., and Worthington, M. H., 1988, The application of diffraction tomography to cross-hole seismic data: *Geophysics*, **53**, 1284–1294.

Reynolds, J. M., 1997, *An Introduction to Applied and Environmental Geophysics*: John Wiley & Sons, 796 p.

Rucker, D. F., and Ferre, T.P.A., 2003, Near-surface water content estimation with borehole ground penetrating radar using critically refracted waves: *Vadose Zone Journal*, **2**, 247-252.

Rucker, D. F., and Ferre, T.P.A., 2004, Correcting water content measurement associated with critically refracted first arrivals on zero offset profiling borehole ground penetrating radar profiles: *Vadose Zone Journal*, **3**, 278-287.

Sacks, Z. S., Kingsland, D. M., Lee, R., and Lee, J. F., 1995, A perfectly matched anisotropic absorber for use as an absorbing boundary condition: *IEEE Transactions on Antennas and Propagation,* **43**, 1460–1463.

Sato, M., and Thierbach, R., 1991, Analysis of a borehole radar in cross-hole mode: *IEEE Transactions on Geoscience and Remote Sensing*, **29**, 899–904.

Sullivan, D. M., 2000, *Electromagnetic Simulation Using the FDTD Method*: IEEE Press, 165 p.

Takahashi, K., and Sato, M., 2006, Parametric inversion technique for location of cylindrical structures by cross-hole measurements: *IEEE Trans. Geosci. Remote Sens.*, **44**, 3348-3355.

Topp, G. C., Davis, J. L., and Annan, A. P., 1980, Electromagnetic determination of soil water content: measurements in coaxial transmission lines: *Water Resources Research*, **16,** 574-582.

Tronicke, J., Holliger, K., Barrash, W., and Knoll, M. D., 2004, Multivariate analysis of cross-hole georadar velocity and attenuation tomograms for aquifer zonation: *Water Resources Research*, **40**, 1519-1532.

Twarakavi, N., Šimůnek, J., and Seo, S., 2007, Evaluating interactions between groundwater and vadose zone using the HYDRUS-based flow package for MODFLOW: *Vadose Zone Journal*, **7**, 757-768.

Washbourne, J. K., Rector, J. W., and Bube, K. P. 2002, Crosswell traveltime tomography in three dimensions: *Geophysics*, **67**, 853–871.

Williamson, P. R., and Worthington, M. H., 1993, Resolution limits in ray tomography due to wave behaviour: *Geophysics*, **58**, 727–735.

Yee, K. S., 1966, Numerical solution of initial boundary value problems involving Maxwell's equations in isotropic media: *IEEE Transactions on Antennas and Propagation*, **14**, 302–307.

Zhou, C., Cai, W., Luo, Y., Schuster, G., and Hassanzadeh, S., 1995, Acoustic wave-equation traveltime and waveform inversion of crosshole seismic data: *Geophysics*, **60**, 765–773.

Acknowledgements

시추공간 레이더에 의한 불포화층의 효율적인 전자기 영상화

장한누리

부경대학교 대학원 에너지자원공학과

요약

지하 투과 레이더는 함수율의 공간적인 분포를 영상화하는 효율적인 수단이다. 시추공간 레이더는 천부 지하를 특성화하고 수리지질학적인 과정을 모니터링 하는데 널리 이용되고 있다. 불포화대에서 함양과정을 조사하기 위해서 인공 지하수 함양 시험을 일본 나가오카에서 수행하였다. 시간 경과에 따른 시구공간 레이더 자료를 zero-offset profiling (ZOP) 모드로 측정하였다. 함양과정은 레이더 주시의 변화로 관측되었으며, 레이더 주시는 유전율로 변환할 수 있으며, 이 유전율은 체적 함수율로 변환 가능하다. 불포화대에서 전자기파 속도의 변화는 함수율의 변화에 크게 의존하기 때문에 주시의 증가는 포화도의 증가로 해석된다.

지하 투과 레이더는 고분해능으로 지하를 영상화하는 효과적인 수단이지만 이와 관련된 고주파수 전자기파의 전파 현상은 복잡하다. 이러한 물리과정을 보다 잘 이해하기 위해서 본 연구에서는 2차원 원통좌표계 맥스웰방정식의 시간영역 유한차분 해를 이용하여 시추공간 레이더 탐사에서의 전자기파 전파형을 효율적으로 모델링 하고자 하였다. 원통좌표계는 전자기파 파동장의 기하학적인 3차원 확산을 정확하게 계산할 수 있으며, 특히 작은 크기의 송신 시추공을 효과적으로 이산화 할 수 있다. 시추공간 레이다 탐사에서 송신 시추공이 전자기파의 전파에 미치는 영향을 확인하기 위해서 전자기 가이드파의 수치모델링을 수행하였다. 그 결과, 물로 채워진 시추공은 강한 도파관 효과를 일으킬 수 있으며, 이 도파관 효과는 시추공의 크기, 안테나의 길이 및 송신 신호의 형태에 의존하는 여러 가지 모드로 구성되어 있음을 확인하였다.

실험 구간에서 배수된 물은 평균 2.7 m/h 로 토양에 침투되었다. 시간영역 유한차분 모델링을 이용하여 포화과정 동안 침윤면의 진행과 관련되는 레이다 기록을 모사하고 임계굴절파의 영향을 정량화 하였다. 모든 초동을 직접파로 가정하고 해석하는 일반적인 ZOP 해석방법은 침윤면 상부의 전이대에서 함수율을 과소평가 하였다. 결과적으로 토양의 함수율 분포를 정확하게 결정하기 위해서 우선 정확한 속도 분석이 수행되어야 하며, 이는 주시단면도 상에서 초동 임계굴절파의 확인을 필요로 한다.

기존의 ZOP 해석 방법은 임계굴절파의 초동을 구별하지 못하기 때문에 이로 인하여 유전율을 과소평가 하게 한다. 그러므로 이 연구에서는 근사적으로 직접파의 주시를 결정하기 위하여 최대 제 1 주기 진폭 (maximum first-cycle amplitude)을 이용하는 효율적인 알고리듬을 소개하였다. 이 알고리듬을 이용하여 추정된 직접파의 주시로부터 기존의 해석방법보다 정확한 유전율을 구하고자 하였다. 합성 예제와 실제 현장자료의 수치실험 결과 이 방법은 많은 시간이 소요되는 반복적인 계산을 하지 않고서도 일반적인 ZOP 해석보다 정확한 함수율 프로파일을 쉽게 얻을 수 있었다.

ZOP 자료로부터 정확한 불포화대의 수리지질학적인 정보를 얻기 위하여 앞서 소개한 해석 방법 보다 정밀한 방법을 소개하였다. 이 방법은 특이치 분해를 이용한 최소자승역산을 기본으로 하며, 2 차원 원통좌표계 시간영역 유한차분 전진 모델링을 전자기 파동장을 계산하는데 이용한다. 이 역산 방법을 합성예제와 현장 자료에 적용하였다. 나가오카 현장에서 함양과정 동안 함수율의 변화를 초동 주시 역산을 이용하여 성공적으로 추정할 수 있었다. 역산 결과로부터 확인되는 포화도 정보는 실험 현장에서 토양의 수리지질학적인 특성을 평가하는데 유용하였다.

주요어: 지중레이더, 시추공간, 시간경과, zero-offset profiling (ZOP), 원통좌표계, 시간영역 유한차분, 불포화대, 유전율, 함수율